

## DC offset leads to saturation of right leg drive output

Zinvi Fu<sup>1,\*</sup>, A.Y. Bani Hashim<sup>1</sup>, Z. Jamaludin<sup>1</sup>, I. S. Mohamad<sup>2</sup>, N. Norazlin<sup>1</sup>

<sup>1)</sup> Faculty of Manufacturing Engineering, Universiti Teknikal Malaysia Melaka, Hang Tuah Jaya, 76100 Durian Tunggal, Melaka, Malaysia

<sup>4)</sup> Faculty of Mechanical Engineering, Universiti Teknikal Malaysia Melaka, Hang Tuah Jaya, 76100 Durian Tunggal, Melaka, Malaysia

\*Corresponding e-mail: zinvifu@yahoo.com

**Keywords:** Right leg drive; DC offset; electric biosignal acquisition

**ABSTRACT** – Due to the high gain that is applied to signal in the right leg drive circuit, the integrity of the RLD signal is easily affected by any direct current (DC) offset present in the RLD circuit. In this report, we have mathematically shown how DC offset affects the RLD output. Then we compared the RLD output with various levels of DC offset. The results show that an offset of 0.1V can saturate the operational amplifier. With a high DC offset, the RLD does not reduce the common mode noise effectively as intended.

### 1. INTRODUCTION

The RLD circuit is used widely in biosignal acquisition circuits, especially in ECG amplifiers [1-2]. The RLD circuit fundamentally consists of an inverting amplifier.

Typically, the RLD amplifier design has a high gain [3]. Therefore, any DC error margin will be amplified as well. If the common mode signal,  $V_{cm}$  and DC offset be  $V_{dc}$ , then the resulting  $V_{RLD}$  in time domain can be expressed in (1).

$$V_{RLD}(t) = V_{cm}(t + \Delta t_A + \Delta t_C) + V_{dc} \quad (1)$$

In practical op-amps, a small phase lag exists at the output [4]. The phase shift due to the op-amp amplification and capacitance are represented by  $\Delta t_A$  and  $\Delta t_C$ . To function effectively, it the RLD circuit must apply as little phase shift and DC offset as possible. However, the effect of DC offset unto the RLD circuit has not been studied extensively in previous literature.

### 2. METHODOLOGY

We have identified three sources of DC offset, which are the electrode offset, resistor tolerance and the default DC offset of gain pins of the instrumentation amplifier itself.

As shown in Figure 1,  $V_{RLD}$  input voltage,  $V_G$ , is taken from the centre tap of the gain resistors  $R_a$  and  $R_b$  which forms a voltage divider. For the high impedance buffer formed by  $R_1$  and  $R_2$ ,  $V_a = V_{in1}$  and  $V_b = V_{in2}$ . Thus the DC output of  $V_G$  can be expressed in (2).

$$V_G = V_{in1} \left[ \frac{R_a}{R_a + R_b} \right] + V_{in2} \left[ \frac{R_b}{R_a + R_b} \right] \quad (2)$$

In an ideal case where  $R_a = R_b = R$ , a symmetrical voltage divider is formed, thus

$$V_G = \frac{1}{2}(V_{in1} + V_{in2}). \quad (3)$$

This equation shows that  $V_G$  is influenced by the difference between  $V_{in1}$  and  $V_{in2}$ . By introducing tolerance into  $R_a$  and  $R_b$ , (3) becomes

$$V_G = \frac{1}{2}(V_{in1} + V_{in2}) - \frac{V_{in1}}{4R} \cdot \Delta R_a + \frac{V_{in2}}{4R} \cdot \Delta R_b. \quad (4)$$

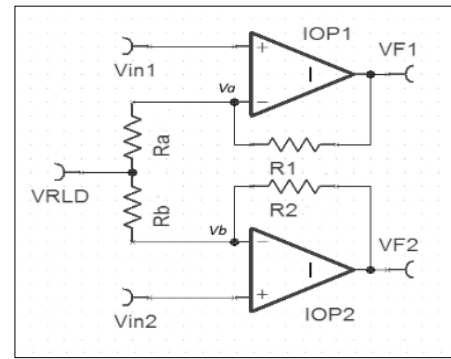


Figure 1 RLD output from instrumentation amplifier.

The deviation of the values  $R_a$  and  $R_b$  due to tolerance are represented by  $\Delta R_a$  and  $\Delta R_b$ . The experimental setup to demonstrate (2) and (3) is shown in 2.

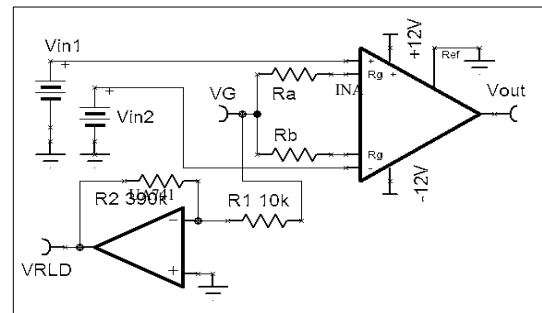


Figure 2 Experimental setup.

The electrode DC offset, represented by  $V_{in1}$  and  $V_{in2}$  are the input. The inverting amplifier with a gain of -39 forms the RLD output. To test the extent of electrode offset difference,  $V_{in1}$  and  $V_{in2}$  were varied between 0-0.5V. Next,  $R_a$  and  $R_b$  were varied within 1% and 5% for the tolerance effect. Finally, with  $V_{in1}$  and  $V_{in2}$  grounded, the integrated amplifier (INA) was measured for DC offset at the VG output.

### 3. RESULTS AND DISCUSSION

The result of  $V_G$  and  $V_{out}$  due to input offset is shown in Figure 3. The half-cell potential of the Ag-Cl electrode is rated at 0.223V. However, this voltage can vary by adhesion, pressure and age of the electrode. For  $V_{out}$ , the differential amplifier rejects common mode input voltage. Hence  $V_{out}$  will trend towards zero when  $V_{in1} = V_{in2}$ , as shown in Figure 4. Unlike  $V_{out}$ ,  $V_G$  averages  $V_{in1}$  and  $V_{in2}$ , thus any DC offset will be amplified as in (3) and (4). For a gain of -39, a 0.1 V DC offset will be amplified to -3.9 V. If the supply voltage is  $\pm 12$  V,  $V_{RLD}$  will go into saturation if the DC offset is above 0.3 V.

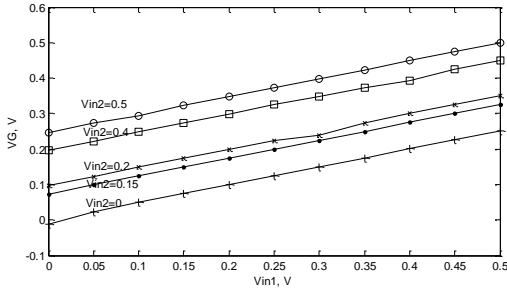


Figure 3 Measured  $V_G$  shift due to DC offset at input.

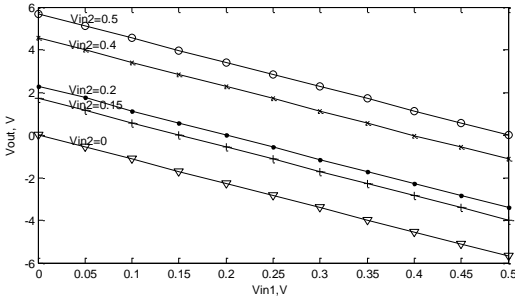


Figure 4 Measured  $V_{out}$  shift due to DC offset at input.

In Figure 5, ten pairs of 1 k $\Omega$  resistors with 1% and 5% tolerance were randomly selected and the resulting  $V_G$  was observed. The deviation of  $V_G$  due to resistor tolerance can be minimized to a negligible level by using 1% tolerance resistors. The default offset of INA114 was measured at -0.0014 V, which results an ideal  $V_G$  of 0.2216 V.

To validate the overall effect of the DC offset at  $V_G$ , the electrodes were connected to the flexor digitorum superficialis muscle. An input filter, as suggested in [5] was applied as a fully calibrated setup against a setup with no input filter. The result in Figure 6 shows that a properly calibrated input filter with negligible offset produces a signal with lower floor noise. For the uncalibrated setup, the  $V_G$  DC offset was allowed to drive the inverting amplifier to saturation. This reduced the effectiveness of the RLD and a higher floor noise was noticeable.

### 4. CONCLUSION

Due to the high gain of the RLD output, any DC offset within its signal chain cannot be tolerated. The objective of this study to shown that DC offset can drive

the RLD into saturation has been demonstrated. The DC offset due to electrode offset is more detrimental than the imbalance voltage divider of  $V_G$ . Therefore, we recommend input filters at the front end and low tolerance resistors for instrumentation gain resistors.

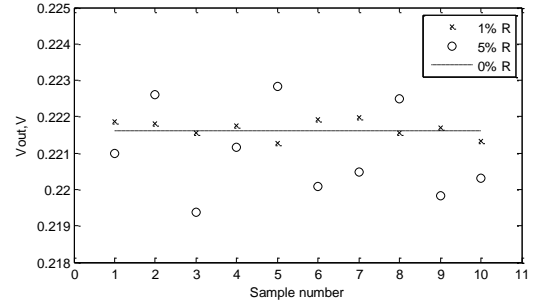


Figure 5 Scatter plot of  $V_G$  deviation due to  $R_a$  and  $R_b$  tolerance.

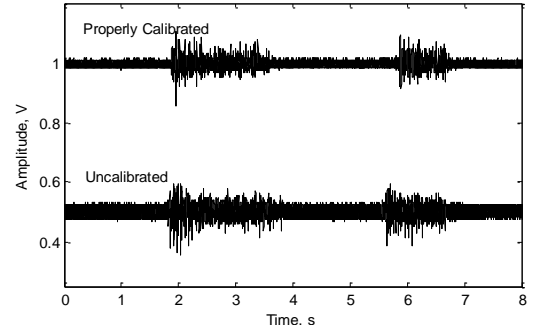


Figure 6  $V_{out}$  with  $V_G$  at zero offset (top) vs  $V_G$  at saturation (bottom).  $V_{out}$  was offset for display purpose.

### ACKNOWLEDGMENT

FRGS/2013/SG02/FKP/02/2/F00176.

### REFERENCES

- [1] A. Wong, K. P. Pun, Y. T. Zhang, and C. S. Choy, "An ECG measurement IC using driven-right-leg circuit," *2006 IEEE Int. Symp. Circuits Syst.*, pp. 345–348, 2006.
- [2] M. Guermandi, E. F. Scarselli, and R. Guerrieri, "A Driving Right Leg Circuit (DgRL) for Improved Common Mode Rejection in Bio-Potential Acquisition Systems," *IEEE Trans. Biomed. Circuits Syst.*, vol. 10, no. 2, pp. 507–517, 2016.
- [3] Y. G. Lim, G. S. Chung, and K. S. Park, "Capacitive driven-right-leg grounding in indirect-contact ECG measurement," *2010 Annu. Int. Conf. IEEE Eng. Med. Biol. Soc. EMBC'10*, pp. 1250–1253, 2010.
- [4] R. Mancini, "Analyzing feedback loops containing secondary amplifiers," 2003.
- [5] C. S. Wang, "A new AC-coupled amplifier for portable ECG without reference electrode," *Comput. Electr. Eng.*, vol. 39, no. 1, pp. 141–149, 2013.

# Fuzzy analytic hierarchy process (FAHP) for better selection during implementation of design for remanufacturing

Ahamad Zaki Mohamed Noor\*, Muhammad Hafidz Fazli Md Fauadi, Fairul Azni Jafar

Faculty of Manufacturing Engineering, Universiti Teknikal Malaysia Melaka,  
Hang Tuah Jaya, 76100 Durian Tunggal, Melaka, Malaysia

\*Corresponding e-mail: ahamadzaki.mohamednoor@gmail.com

**Keywords:** Fuzzy analytic hierarchy process; design for remanufacturing; economy indicator

**ABSTRACT** – Design of Remanufacturing consist of three indicators namely social, environment and economical. In this paper, economic indicator is improved by implementing FAHP during cost selection. Therefore, the decision is made by placing weightage in term of distance and cost. It is observed that Option 2 is the best followed by option with FAHP. The results obtained portray slightly different in which Option 2 is cheaper than Option 1 in term of insurance payment for one year. But if were to revise the calculation the reasoning behind the selection of 5 years payment is cheaper than one year. Future work is to apply this FAHP findings combine tool with Neural Network and apply it in Design for Remanufacturing.

## 1. INTRODUCTION

Design for Remanufacturing(DFR) is a concept of manufacturing environment which are developed currently for future generation of manufacturing and process technology. Remanufacturing is a process of returning used product by rework, disassemble, reassemble, reprocess, inspect and testing in order to return its appearance to brand new part [1]. Several importance elements that are inter-related include from selection of machine, maintenance, labour, direct and indirect costs. Through remanufacturing, the essential values for components or parts can be sustained. Reprocessed quality is assured for the next life cycle [2]. Problem with current practice which is product can be reuse or recycle rather than place as scrap. This will however produce waste in term of energy, inventory, time and other lean factors. Some variable may have other alternative to be substitute in economic indicator. Therefore, the need to identify option suitable before finalize in the economic indicator is crucial. In order to solve these problems, FAHP into DFR will be made to

## 2. METHODOLOGY

The quantitative measurement is being done only for economic indicator. The method is carried out by gathering data needed for variables in DFR. The data consists of three options representing several variables that are involved in economy variable's equation. FAHP is proposed to determine the best option in order to be substituted in formula of DFR. Once the best options for every cost are decided, the price value of the option will be substituted in economy equations. Two different answers will be obtained after computation whereby the current economy result, and after proposed method result. These answers are grouped and organized to determine which option produces the best price value. The justification of results is made after obtaining the results. Overall methodology is shown in Figure 1.

## 3. RESULTS AND DISCUSSION

For insurance cost, Insurance C is selected due to longer period coverage and cheaper if calculate per year. Insurance B offer RM 79 per year however Insurance C offers RM 359 for 5 years which is RM 36 cheaper. It is more profitable if 5 years insurance package is selected rather than renew every year Figure 2 is the scaling result of criteria for insurance cost.

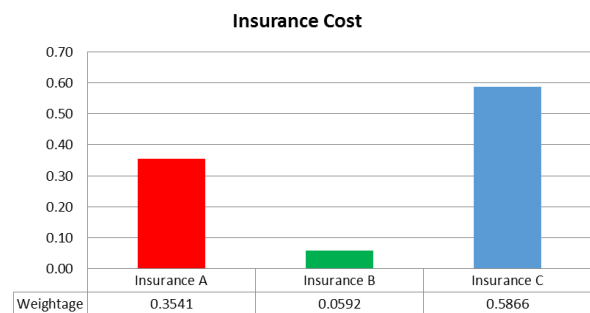


Figure 2 Weightage of insurance cost.



Figure 1 Overall methodology.

In terms of direct overhead cost, it shows that option 2 is the best selection due to cheap in material and labor cost, best material handling and providing shortest distance. Figure 3 shows the weightage of direct overhead cost.

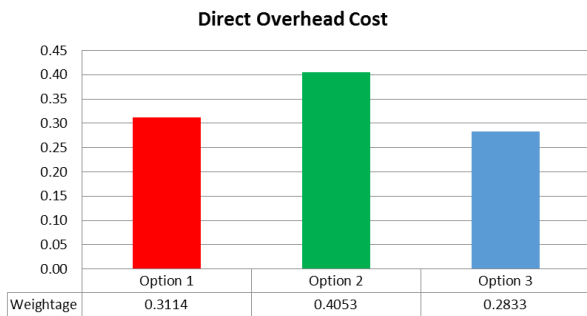


Figure 3 Weightage of direct overhead cost.

For indirect overhead cost, total salaries, expenses show cheapest compared to option 1 and 3. Figure 4 shows the weightage whereby option 2 is the best selection.

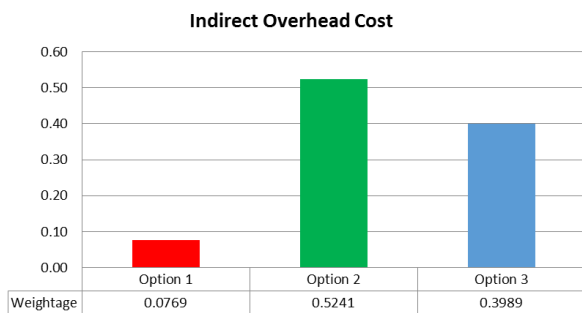


Figure 4 Weightage of indirect overhead cost.

Figure 5 shows that supplier 3 is the best selection if were made due to better material type and nearby distance.

Transport 1 is selected because the products are not so big and does not need big space and transport 1 have the cheapest rental cost for transport. Figure 6 shows weightage of transport cost.

For packaging cost, the highest weightage is at package 3 due to cheapest price. Figure 7 shows weightage of package cost.

Once all have been scaled, the best option is determined, insurance of machine should be covered cheap and have longer time. The same goes for direct, indirect overhead, spare part, transport and packaging cost needed to be cheaper. Some may want the supplier to be nearer to plantation. However, some supplier provides cheap yet the distance is far from factory. The proposed method is done by selecting best option and labeled it as "with FAHP". To summarize the final answers after substitution in the economy indicator's equations, Figure 8 represents all the option in a form of bar chart.

From Figure 8, shows that Option 2 and option with FAHP have almost same profit which are RM 1,302 and RM 1,249. All options show that they are

profitable however the differences made by these two options are from the insurance sector.

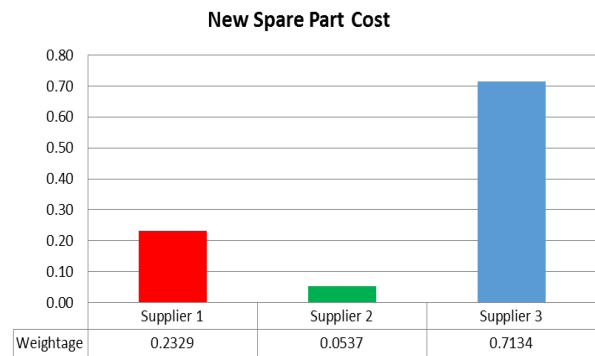


Figure 5 Weightage of new spare part cost.

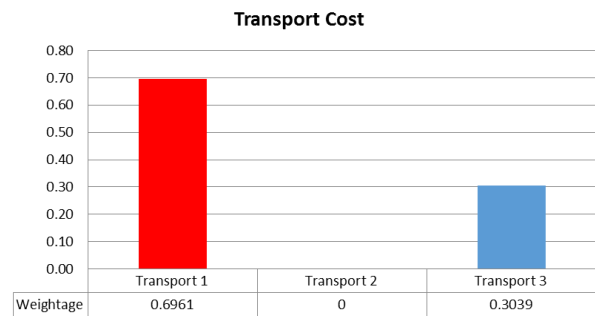


Figure 6 Weightage of transport cost.

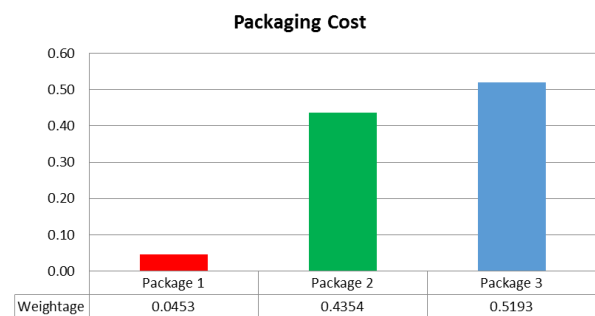


Figure 7 Weightage of packaging cost.

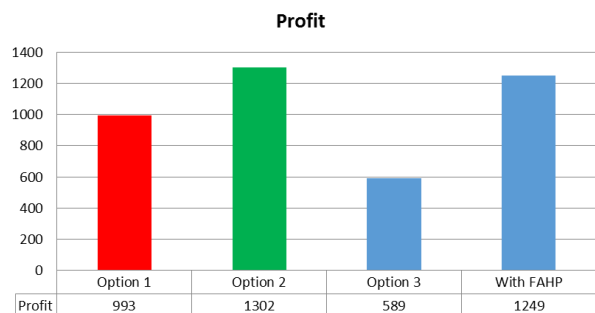


Figure 8 Comparison profit between 4 options.

#### 4. CONCLUSION

In conclusion, in order to attain sustainable in manufacturing layout, best or almost best option needed to be identified and FAHP have done a great job for that.



To conclude, FAHP is feasible to be executed which solve multi alternatives and create profit to company by implementing Design for Remanufacturing.

## REFERENCES

- [1] G. D. Hatcher, W. L. Ijomah, and J. F. C. Windmill, "Design for remanufacturing in China: a case study of electrical and electronic equipment," *J. Remanufacturing*, vol. 3, no. 1, p. 3, 2013.
- [2] S. S. Yang, N. Nasr, S. K. Ong, and A. Y. C. Nee, "Designing automotive products for remanufacturing from material selection perspective," *J. Clean. Prod.*, 2015.

# Modeling and PID controller design using optimization technique for pneumatic system

Khairuddin Osman\*, Muhammad Fahmi Faujan, Azira Abd Rahman, Siti Fatimah Sulaiman

Faculty of Electronics and Computer Engineering, Universiti Teknikal Malaysia Melaka,  
Hang Tuah Jaya, 76100 Durian Tunggal, Melaka, Malaysia

\*Corresponding e-mail: khairuddin.osman@utem.edu.my

**Keywords:** Proportional integral derivative; particle swarm optimization algorithm; harmony search algorithm

**ABSTRACT** – Proportional Integral Derivative (PID) controllers is prominent controllers used in industry due to its remarkable effectiveness in term of producing, simplicity of implementation and broad applicability. However, tuning of this controllers is time consuming, effortful and thus, it may lead to poor performance especially with non-linear systems. A linear parametric model of ARX is constructed based on system identification to overcome the modeling complexity. A discrete PID controller has been applied to track the desired position. Particle Swarm Optimization (PSO) algorithm and Harmony Search Algorithm (HAS) applied in controllers to optimize the controller's parameter. Both optimization algorithm was produced the best value of proportional gain, integral gain and derivative gain. Each optimization was suggesting three suitable gains for PID controller in order to achieve best performance. The tracking performances of controller based on both optimizations are compared between simulations and real-time. The validation of real-time is executed by comparing the experimental results with simulation results of load effect.

## 1. INTRODUCTION

Pneumatic cylinder systems have become an element widely used in machinery, automation and industrial robotics. Good power-to-weight ratio, high maximum forces and excellent flexibility are their key attributes [1].

Proportional Integral Derivative (PID) controller, which will be the focus of this study for the positional control of this pneumatic system, wins over the other controllers due to its lower overshoot and faster response as time increases.

To optimize the controller parameters, a few algorithms can be applied, for example, Harmony Search Algorithm (HSA), Ant Colony Optimization (ACO), Particle Swarm Optimization (PSO), Simulated Annealing (SA), Genetic Algorithm (GA), Gravitational Search Algorithm (GSA) and Bat Algorithm (BA). These algorithms are inspired by nature and meta-heuristic methods adapted by physical phenomenon. A common point in meta-heuristic algorithm is that it combines rules and randomness to mimic natural phenomenon.

The PSO algorithm is an algorithm that is based on a concept of population based search algorithm working

on the simulation of social behaviour of birds in a flock [2]. The capability of HSA optimization technique is it can develop better arrangements compared to other existing optimization in less number of iterations [3].

## 2. METHODOLOGY

The rest of this paper is organized as follows are the position model of the pneumatic, optimization parameter determination and tuning parameter strategies, analysis simulation and experimental results of the tracking performance of the system.

Figure 2 shows overall parts of the pneumatic actuator. The pneumatic system is equipped with two sensors such as optical sensor and pressure sensor. Optical sensor was used where smaller pitch of 0.01 mm is able to be detected. Two miniature valves are attached at the end of the cylinder. The actuator has 200 mm stroke and capable to provide maximum force up to 120 N.

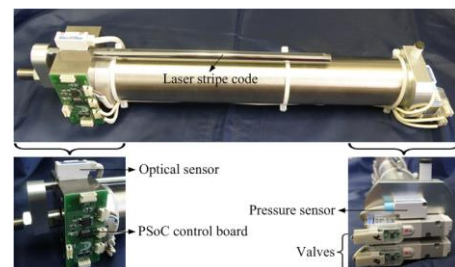


Figure 1 Pneumatic system and its parts.

Position model proposes continuous step input signal which is applied to pneumatic actuator system for model estimation. The following third order Auto-Regressive with Exogenous Input (ARX) model in the form of discrete-time open-loop for position transfer function was obtained as presented in Equation (1).

$$\frac{B_{Position}(z^{-1})}{A_{Position}(z^{-1})} = \frac{0.001269z^{-1} + 0.0004517z^{-2} - 0.0003498z^{-3}}{1 - 1.932z^{-1} + 1.09z^{-2} - 0.1577z^{-3}} \quad (1)$$

The Parameters of PSO had been set after many times keep repeating change variable listed in Table 1 while the HSA parameters were set listed in Table 2. The method for tuning the HSA optimization is referred to [4] and PSO optimization is referred to [5].

Table 1 PSO parameters.

No.	Parameter Description	Values
1	Number of Iteration, $N_t$	10
2	Number of Dimension, $N_d$	3
3	Number of Particle, $N_p$	100
4	Inertia Weight, $i_w$	0.9
5	Cognitive Component, $c$	1.42
6	Social Component, $s$	1.42
7	Upper Boundary, $u_p$	100
8	Lower Boundary, $l_p$	0

Table 2 HSA parameters.

No.	Parameter Description	Values
1	Number of Iteration, $N_t$	10
2	Number of Dimension, $N_d$	3
3	Number of Harmony Memory, $N_{hm}$	100
4	Pitch Adjusting Rate, $R_{pa}$	0.5
5	Harmony Memory Rate, $R_{hm}$	0.8
6	Rate of Global, $R_g$	0.1
7	Upper Boundary, $u_B$	100
8	Lower Boundary, $l_B$	0

The load test had been testing for 1 Kg, 2 Kg, 3 Kg, 4 Kg and 5 Kg. Every load testing came out with different output response. The plate load will give effect to pneumatic actuator model in term of vibration and stability.

### 3. RESULTS AND DISCUSSION

For this study, the PSO and HSA are used as a method of optimization for pneumatic cylinder actuator system. Both optimizations were come out with different of proportional gain, integral gain and derivative gain after complete iteration of those algorithms. Figure 2 shows simulation of both PSO and HSA output response while Figure 3 and Figure 4 shows the real time experiments output response respectively.

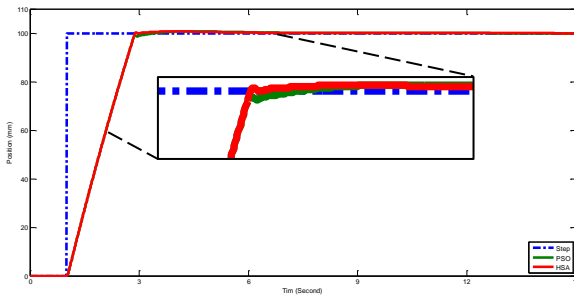


Figure 2 HSA and PSO simulation.

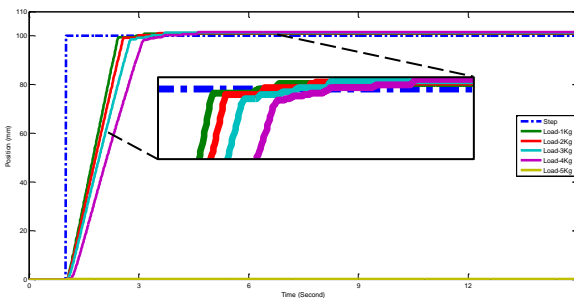


Figure 3 Real-Time PSO with load output response.

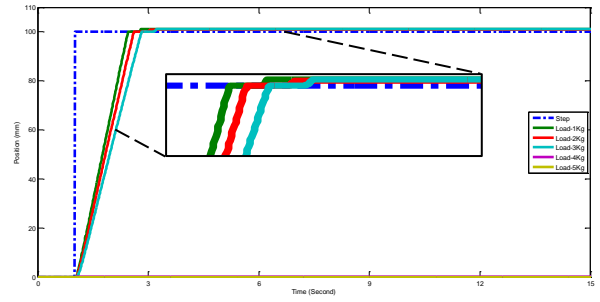


Figure 4 Real-time HSA with load output response

The Particle Swarm Optimization produce  $K_p = 80.3202$ ,  $K_i = 90.5367$  and  $K_d = 10.3981$  while for Harmony Search Algorithm produce  $K_p = 85.2091$ ,  $K_i = 97.4836$  and  $K_d = 6.6946$ . Those best gain were come out the possible output response in simulation and real-time. Means, those gains were acceptable to be use on third order linear transfer function of the pneumatic cylinder actuator.

### 4. CONCLUSION

The developing an optimization technique for PID controller and measure the performance both simulation and real-time using optimized were successfully work. The validation experimental load effect has been completely explained in detail.

### ACKNOWLEDGEMENT

The authors would like to thank Universiti Teknikal Malaysia Melaka (UTeM) and Ministry of Education (MOE) Malaysia under the Research Acculturation Grant Scheme (RAGS) No. RAGS/1/2014/TK03/FKEKK/B00063 for their support.

### REFERENCES

- [1] Rahmat, M.F. and Kamaruddin, N.S., Application of fuzzy logic and electrodynamic sensors as flow pattern identifier. *Sensor Review*, vol. 32, no. 2, pp.123-133, 2012.
- [2] Eberhart, Russ C., and James Kennedy. "A new optimizer using particle swarm theory." In *Proceedings of the Sixth International Symposium On Micro Machine and Human Science*, vol. 1, pp. 39-43. 1995.
- [3] Kougias, I., and N. Theodossiou. "A new music-inspired harmony based optimization algorithm. Application in water resources management problems." In *Proceedings of the PRE X International Conference*, vol. 59. 2010.
- [4] Osman, Khairuddin, Ahmad Athif Mohd Faudzi, M. F. Rahmat, Amar Faiz Zainal Abidin, and Koichi Suzumori. "Proportional-integrative controller design of Pneumatic system using particle swarm optimization." In *IEEE Student Conference on Research and Development*, pp. 421-426, 2013.
- [5] Geem, Z.W., Kim, J.H. and Loganathan, G.V., "A new heuristic optimization algorithm: harmony search," *Simulation*, vol. 76, no. 2, pp.60-68, 2001.

# Electromyography signals analysis using wavelet transform approach for resistance band rehabilitation

N. Burhan<sup>1</sup>, R. Ghazali<sup>1,\*</sup>, M.A. Kasno<sup>2</sup>, M.H. Jali<sup>1</sup>

<sup>1</sup>) Faculty of Electrical Engineering, Universiti Teknikal Malaysia Melaka, Hang Tuah Jaya, 76100 Durian Tunggal, Melaka, Malaysia

<sup>2</sup>) Faculty of Engineering Technology, Universiti Teknikal Malaysia Melaka, Hang Tuah Jaya, 76100 Durian Tunggal, Melaka, Malaysia

\*Corresponding e-mail: rozaimi.ghazali@utem.edu.my

**Keywords:** Wavelet transform; electromyography; rehabilitation analysis

**ABSTRACT** – Electromyography (EMG) signals analysis is one of the important techniques to investigate rehabilitation exercises. However, the signal is highly nonlinear that required appropriate method to extract the accurate features. This paper presents an analysis of the EMG signals of human biceps brachii muscle that is applied in resistance band rehabilitation. There are three level of movements during the rehabilitation exercise where the EMG signals will be recorded during contraction condition of the biceps brachii muscle. In the experimental works, EMG signals are acquired by using wavelet transform approach to analyze the rehabilitation process. It is found that the proposed technique is capable to represent the EMG signals effectively as one of the significant feature extraction.

## 1. INTRODUCTION

Electromyography (EMG) is one of the biomedical techniques concerned about the recording, analysis, and development of myoelectric. The myoelectric signals also referred as the EMG signals where it is formed by small electrical currents during muscle contraction. The signals can be acquired from the arm skin surface which is detected by using surface EMG electrodes. Basically, there are two types EMG signals to be collected which namely, surface EMG (sEMG) and needle EMG. Mostly, researchers utilized sEMG electrodes since it is a non-invasive method where it is more convenience and suitable to apply without any medical certificate. The sEMG has been assigned as an input in various applications such as biomedical applications, rehabilitation robotics and prosthetics arm as an assistant for human muscle detection activities during contraction and relaxation. It is also able to provide the significant control input for those applications.

In this paper, Wavelet Transform (WT) technique will be proposed in time-frequency domain using sEMG signal processing. This technique is applied to extract the main features of the EMG signal.

## 2. METHODOLOGY

In the experiment, there are several procedures that need to be executed before apply the sEMG electrodes where human skin need to be cleared from any hair and exfoliating. Then, the skin will be cleaned with 70% Isopropyl Alcohol. It will reduce unnecessary of noise

and help the user to obtain the best EMG signals with the minimize noise.

This experiment will be conducted with three different levels by using the resistance band rehabilitation exercise. The volunteered for this study must be in healthy condition and have normal of body mass index (BMI). The volunteered were ask to perform three levels of biceps brachii muscle contraction and the same weight of mass which is 16 kg. These levels are conducted at angle 30°, 90° and 150° as shown in Figure 1.

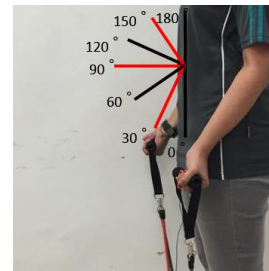


Figure 1 Maintaining the load at 30°, 90° and 150°.

After acquired the EMG signal for each level that had been set, the EMG signals still contain noises and it will be removed by the feature extraction method. There are two important parts that need to be highlight in feature extraction which is the first part is to remove baseline wandering by using WT approach which is effective ways to remove signals within specific subbands. The LabVIEW Advanced Signal Processing Toolkit (ASPT) will provide the WA Detrend VI that useful for remove the low-frequency trend of a signal. The second part is removing wideband noise that user can use Wavelet Denoised Signal in LabVIEW. These steps is crucially important to produce less or noise-free EMG signal. This approach is then applied to the virtual instrument (VI) in LabVIEW to real time signals.

## 3. RESULTS AND DISCUSSION

The EMG signals of biceps brachii muscle were recorded during contraction for three levels of arm movements which are at angle 30°, 90° and 150°. The original EMG signal recorded contained several noises such as motion artifact, inherent noise, ambient noise, cross-talk and internal noise.

In the LabVIEW program, the virtual instrument

applied a discrete wavelet transform (DWT) to the input for performing low-pass and high-pass filtered at each level to produce wavelet transform [1].

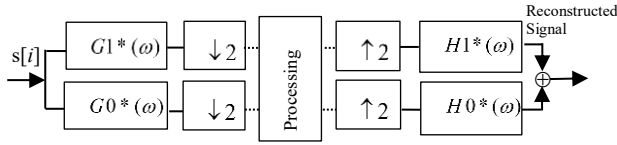


Figure 2 The discrete wavelet transform through two-channel perfect reconstruction filter banks.

Based on Figure 2, the EMG signals acquired will be filtered by a perfect reconstruction filter banks that consist of low-pass filters ( $G_0$  and  $H_0$ ) and high-pass filters ( $G_1$  and  $H_1$ ). The input signal will pass through ( $G_0$  and  $G_1$ ) and then downsampled by a factor of 2. After that, it will continue with some processing and the modified signals will be upsampled by a factor of 2. The low-pass filters will remove the high-frequency signals and keep remain the slow trend while the high-pass filters will keep remain the high-frequency signals and remove the slow trend.

In this experiment, the EMG signals were decomposed into details from D1 until D4 and use the db2 of Daubechies Wavelets to fourth levels where it proved the effectively by other researchers. After that, the EMG signals at detrend stage will proceed to the feature extraction method which is wavelet denoise. The EMG signal acquired will filter using wavelet transform technique in wavelet denoise which having selected the parameters in wavelet transform selection in term of mother wavelet and decomposition levels, threshold selection algorithm and rescaling function.

In wavelet basis function, the db4 Daubechies Wavelet had been chosen as the mother wavelet and 10<sup>th</sup> decomposition level. A recent work had been exploited that the best mother wavelet is Daubechies 4 (db4) which the most effective analysis in EMG signals compared with other Daubechies Wavelet where it might be able loss EMG signal information [2]. The chosen of the threshold selection rules for this experiment is a hybrid method which removes more coefficient about 7 level to 10 levels compared other which only fewer coefficient involved. Other than that, the hybrid method also is the best removing noise from the EMG signal. The EMG signals after removing baseline wandering after wavelet denoised for three different arm levels can be seen in Figure 3, Figure 4, and Figure 5.

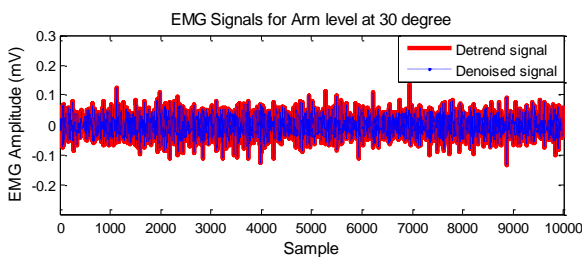


Figure 3 EMG signal for arm level at 30 degrees.

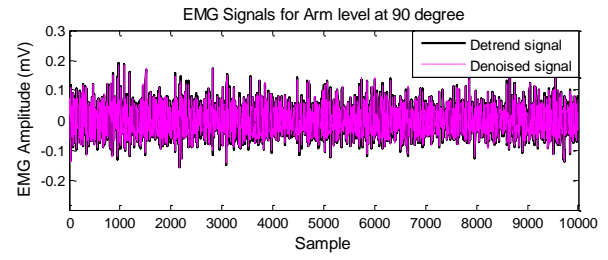


Figure 4 EMG signal for arm level at 90 degrees.

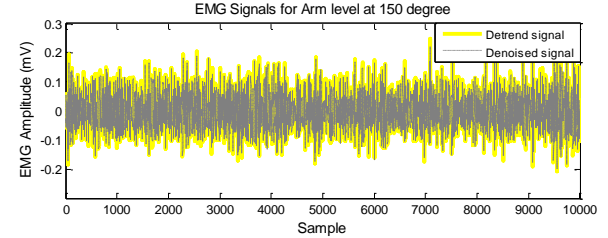


Figure 5 EMG signal for arm level at 150 degrees.

Analysis for these exercises is done on different EMG signals acquired from the different level of arm movements with rehabilitation resistance band. Based on the results, it is found that the Discrete Wavelet Transform technique is capable to distinguish the raw signal based on the different level of arm movements. This is one of the essential attribute for features extraction selection.

#### 4. CONCLUSION

The aim of this paper is to propose researchers to focus on the wavelet transform features that able to extract from the EMG signal during performing three levels of arm movement by using resistance band in rehabilitation application. The result shows that the amplitude of the EMG signal is increased when the maximum contraction of muscle achieved at angle 150°. After performing EMG denoised by applying WT technique, the result shows slightly difference compared with the EMG signals produced after denoised is not lost too much the details and the important information in the signals. Therefore, it can be conclude that the proposed technique has a good capability to extract features of the EMG signal.

#### ACKNOWLEDGEMENT

Grant No.: RAGS/1/2015/TK05/FTK/03/B0012.

#### REFERENCES

- [1] A. Attenberger, E. Andreasattenbergerunibwde, and K. Buchenrieder, "Wavelet-Based Detrending for EMG Noise Removal," *20th Annu. IEEE Int. Conf. Work. Eng. Comput. Based Syst. Wavelet-Based*, pp. 196–202, 2013.
- [2] D. Gradolewski, P. M. Tojza, J. Jaworski, and D. Ambroziak, "Arm EMG Wavelet-Based Denoising System," *J. Awrejcewicz al. (eds.), Mechatronics Ideas Ind. Appl. Adv. Intell. Syst. Comput.* 317, pp. 289–296, 2015.

# Nondestructive evaluation and optimization of composite material CFRP/GFRP layup

N.A.A. Md Zahir\*, M.A.M. Daud, A.F. Ab Ghani<sup>1</sup>

Faculty of Mechanical Engineering, Universiti Teknikal Malaysia Melaka,  
Hang Tuah Jaya, 76100 Durian Tunggal, Melaka, Malaysia

\*Corresponding e-mail: aizatul\_ain92@yahoo.com

**Keywords:** Composite optimization; CFRP; GFRP

**ABSTRACT** – The article presents a parametric studies of different arrangement of combined composite carbon fiber reinforced polymer/glass fiber reinforced polymer (CFRP/GFRP) in determining mechanical properties of modulus of elasticity. Apart from value of A11 (extensional stiffness), other mechanical properties such as B11 (extensional-bending coupling) and D11 were also computed. It is performed analytically using MATLAB version R2012b and validated by using eLamX2 software. The outcome of the analytical simulations shows that, the higher number of CFRP ply in composite laminate, the higher elastic modulus. Bending stiffness of composite laminates also increase if CFRP ply position is at the outermost of composite laminates.

## 1. INTRODUCTION

Composites material have been known for their ability replacing the conventional material because of their higher strength-to-weight ratio, tailored design, corrosion resistant, etc. Although replacing metal to fully carbon fiber may be advantageous in higher strength-to-weight ratio, however this method involved high production cost. Thus, another method that can be look at is by producing Hybrid Fiber Reinforced Polymer (HFRP) with adding GFRP into high modulus unidirectional CFRP. Producing a HFRP from higher modulus unidirectional CFRP and GFRP beam, is perhaps more reliable means of enhancing its flexural stiffness [1].

Flexural stiffness and strength of horizontally glued laminated wood beams with GFRP and CFRP composite sheets is increased compared to unstrengthened wood beam [2]. This study shows that in order to strengthening laminated wood beams, FRP proved to be efficient reinforcement material. For flexural strengthening of concrete beams using CFRP, GFRP and hybrid FRP sheets, GFRP is found to be good material for strengthening because of its high deformability, good impact and break resistance properties compensate with its lower elastic modulus than carbon fiber [3].

## 2. METHODOLOGY

In order to analyze the elastic properties for entire laminates, Classical Laminates Theory is applied and ABD matrix (or laminate stiffness matrix) which consist of 6 x 6 matrix serves as a tool to define these properties. Matrix A is extensional, B is coupling and D is bending

stiffness of the lamina/laminates. The basic concept for underlying the fiber reinforced composite material are stiffness and strength thus, the output that concern in this study is A11 since it is an important parameter for extensional stiffness in longitudinal direction. The mechanical properties are based on Cytec Material Database in Table 1 as follows:

Table 1 Material database for CFRP and GFRP.

Properties	CFRP	GFRP
Longitudinal elastic modulus, E1 (GPa)	128.80	45.20
Transverse elastic modulus, E2 (GPa)	9.30	14.10
Major Poisson's ratio, V12	0.34	0.29
Shear Modulus, G12 (GPa)	3.37	6.30
Thickness per layer (mm)	0.45	0.14

### 2.1 Calculation ABD matrix

Nine different cases with different number of CFRP and GFRP, different arrangement and same fiber orientation of 0° is studied. MATLAB function is required to develop the ABD matrix that calculated from mechanical constant properties of each ply based on Table 1. The calculation for ABD matrix starting with determination of reduced stiffness, Q for every layup as shown in Figure 3 followed by ABD matrix computation using the setup function. The matrix components for A<sub>ij</sub>, B<sub>ij</sub>, and D<sub>ij</sub> are calculated using the following equations:

$$A_{ij} = \sum_{k=1}^n I(\bar{Q}_{ij}) J_k (h_k - h_{k-1}) \quad (1)$$

$$B_{ij} = \frac{1}{2} \sum_{k=1}^n I(\bar{Q}_{ij}) J_k (h_k^2 - h_{k-1}^2) \quad (2)$$

$$D_{ij} = \frac{1}{3} \sum_{k=1}^n I(\bar{Q}_{ij}) J_k (h_k^3 - h_{k-1}^3) \quad (3)$$

Where h<sub>k</sub> refer to the bottom boundary whereas h<sub>k-1</sub> is upper boundary for composite layup. Figure 1 shows all the cases of composite laminates involved. Red region indicated CFRP layup whereas yellow region indicated GFRP layup in composite laminates.



	Case 1	Case 2	Case 3	Case 4	Case 5	Case 6	Case 7	Case 8	Case 9
Layer 1									
Layer 2									
Layer 3									
Layer 4									
Layer 5									
Layer 6									
Layer 7									
Layer 8									
Layer 9									
Layer 10									
Layer 11									
Layer 12									

Figure 1 Nine cases for composite laminates.

As the composite laminates behave in orthotropic ways, the relationship between stress and strain involved four elastic constants ( $E_1$ ,  $E_2$ ,  $G_{12}$ , and  $\nu_{12}$ ). The result obtained from MATLAB calculation is then validated by another composite laminate calculation software which is eLamX2 as shown in Figure 2. The results obtained from both MATLAB and eLamX2 software is same thus suggest that the result is valid.

ABD-Matrix						
142.9	5.2	0.0	0.0	0.0	0.0	0.0
5.2	16.5	0.0	0.0	0.0	0.0	0.0
0.0	0.0	6.6	0.0	0.0	0.0	0.0
0.0	0.0	0.0	32.5	0.8	0.0	0.0
0.0	0.0	0.0	0.8	2.5	0.0	0.0
0.0	0.0	0.0	0.0	0.0	0.0	0.9

Figure 2 Example of eLamX2 as validation tool.

### 3. RESULTS AND DISCUSSION

The factor that been looked at in this study is the modulus of elasticity of composite laminates in longitudinal direction,  $E_{11}$  which calculated by using equation below:

$$E_{11} = \frac{\text{Extensional Stiffness in 1-direction, } A_{11}}{\text{Total thickness of laminates, } H} \quad (4)$$

The result obtained is tabulated as in Table 2. For all cases studied,  $A_{11}$  is increasing proportionally with the increase of CFRP layup in the laminates. This is due to the fact that the higher of extensional stiffness of CFRP that contribute to the high extensional modulus of composite laminates than GFRP.

In this present study, the longitudinal direction (or 1-direction) is concerned thus highlighted on  $A_{11}$ ,  $B_{11}$ , and  $D_{11}$  value which obtained from equation (1), (2), and (3). From mechanical properties perspective,  $A_{11}$  is related to the deformation for composite laminates which equivalent to the extensional modulus in longitudinal direction,  $E_{11}$  [4]. B matrix components for all cases is zero due to symmetrical laminate arrangement.  $D_{11}$  represent the bending stiffness in 1-direction, which correspond to the radius of the curvature of laminates [4].

Some cases (Case 4/Case 9 and Case 7/Case 8) shown same value of  $A_{11}$  but different value in  $D_{11}$ . This is because they have equal number of CFRP and GFRP plies in laminates that will produce equal extensional stiffness. However,  $D_{11}$  for Case 4 is higher than Case 9 and  $D_{11}$  for Case 8 is higher than Case 7. The reason is the position of CFRP layup from the midpoint since the further position of CFRP from midpoint will increase bending stiffness and result in smaller curvature in composite laminates. Higher  $D_{11}$  relates to higher bending stiffness and resistance to bending deformation.

Table 2 Result for ABD matrix.

Properties	No of CFRP	No of GFRP	Total Thickness (mm)	$E_{11}$	$A_{11}$	$D_{11}$
Case 1	2	3	1.46	97.87	142.89	32.46
Case 2	3	4	1.92	105.54	202.64	70.08
Case 3	4	5	2.50	105.84	264.61	166.52
Case 4	2	6	1.74	89.59	155.89	40.81
Case 5	1	6	1.29	75.53	97.44	8.94
Case 6	1	10	1.85	66.72	123.43	25.13
Case 7	2	8	2.02	83.60	168.88	52.31
Case 8	2	8	2.02	83.60	168.88	79.44
Case 9	2	6	1.74	89.59	155.89	34.79

### 4. SUMMARY

The present study shows variation of combined CFRP/GFRP composite where each case yields different set of mechanical properties. Several laminates having similar number of CFRP, but having different arrangement will yield different  $D_{11}$  although equal value of  $A_{11}$ . Increasing number of CFRP significantly improved the overall  $A_{11}$  of the combined composite and it is found that reducing single CFRP and increasing single GFRP (case 2 and case 3) will yield quite similar computation of  $E_{11}$  (within 3% deviation). Positioning of CFRP at outer/external layers and inner layers will not affect the computation of value of  $A_{11}$  based on case 7 and case 8 as well as case 4 and case 9.

### REFERENCES

- [1] G.J. Turvey, "CFRP stiffened GFRP continuous beams – A simple closed-form analysis and its experimental verification for serviceability limit deformations," *Composite Structure*, vol. 153, pp. 952–960, 2016.
- [2] Y. Nadir, P. Nagarajan, M. Ameen, and M. Arif, "Flexural stiffness and strength enhancement of horizontally glued laminated wood beams with GFRP and CFRP composite sheets," *Construction and Building Materials*, vol. 112, pp. 547–555, 2016.
- [3] N. Attari, S. Amziane, and M. Chemrouk, "Flexural strengthening of concrete beams using CFRP, GFRP and hybrid FRP sheets," *Construction and Building Materials*, vol. 37, pp. 746–757, 2012.
- [4] N. Pan, J. Wu, K. Williams, and Y. Wang, "Effects of floor coverings on posture steadiness and locomotion stability," *National Textile Center Annual Report*, S04-CD03, 2004.

# Determination of the optimal workspace and manufacturing throughput time for configuring robot work cell

N.S., Osman, M.A.A. Rahman\*, A.A. Abdul Rahman, S.H. Kamsani, B.M.B. Mohamad

Advanced Manufacturing Centre, Faculty of Manufacturing Engineering, Universiti Teknikal Malaysia Melaka, Hang Tuah Jaya, 76100 Melaka, Malaysia

\*Corresponding e-mail: arfauz@utem.edu.my

**Keywords:** Optimum robot work cell; workspace area; manufacturing throughput time

**ABSTRACT** – This paper elaborates the concept of optimal configuration which involves the formulation of mathematical models of workspace area,  $A_w$  and manufacturing throughput time,  $MTT$  for the robot work cell. The aim of this work is to provide rapid configuration process which is the optimal layout,  $L_{opt}$  of robot work cell is determined. An optimal configuration concept with its mathematical models have been developed based on the variant-shaped robot layout. The current outcome of this work will provide a basis for future investigation in developing computer-based configuration system.

## 1. INTRODUCTION

Laying out the multiple robot work cell has received considerable attention in the last few years [1-5]. Nevertheless, most of the recent configuration work i.e. in [1-4] only concerned to the design or/and mathematical model regardless the optimization approach which the approach will be discussed in this paper. The significant of involving this approach is to obtain the optimal cell layout where it yields a desired manufacturing strategy. The earliest work on configuring the multiple robots based on the variant-shaped layout as depicted in Table 1 and 2 are taken as a reference.

Table 1 Variant-shaped layout.

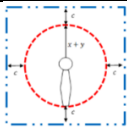
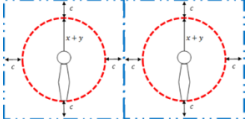
Number of Robot, $N_r$	Robot Work Cell Layout	Number of Configuration, $N_c$
1		1
2		1

Table 2 Variant-shaped configuration layout data.

Number of Robot Used, $N_r$	1	2	3	4	5	6	7	8	9	10
Number of Configuration, $N_{c,initial}$	1	1	2	5	12	35	108	369	1285	4655

The variant-shaped layout is developed in a simple arrangement of spatial geometry that is formed by joining one or more equal squares side by side without

considering rigid transformation condition (translation, rotation, reflection or glide reflection). This paper presents the approach to solve the earlier mentioned issue by formulating the optimization concept, emphasizes on the workspace area,  $A_w$  and manufacturing throughput time ( $MTT$ ) which is based on the developed variant-shaped layout. This outcome will assist in determining the optimal layout,  $L_{opt}$  of the robot work cell.

## 2. METHODOLOGY

The primary development processes include for determining the workspace and the manufacturing throughput time. They are presented in three separate sections as follows:

- 1) **Identify Specification Robot:** This includes reviewing and analyzing the workspace and manufacturing throughput time specifications as well as the constraints and conditions.
- 2) **Design Multiple Robot:** This stage involves modelling the concept of workspace and manufacturing throughput time for the multiple robot work cell.
- 3) **Determine Optimum Multiple Robot:** This stage represents the mathematical equation in selecting the optimum layout based on the developed concept in stage 2.

## 3. RESULTS AND DISCUSSION

### 3.1 Workspace of robot work cell

The specifications of robot workspace introduced by Rahman work are taken as reference where two dimensional robot work cell (Figure 1) and its safety working area,  $A_{safe}$  in equation (1) are employed [5].

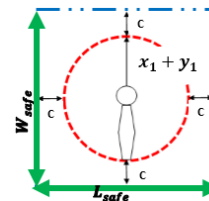


Figure 1 Illustration of a safe robot work cell [5].

$$A_{safe} = L_{xsafe} \times L_{ysafe} = 2(x + y + c) \times 2(x + y + c) \quad (1)$$



Where;  $x$ : Length of the robot arm (mm)  
 $y$ : Length of the robot tooling and work piece (mm)  
 $c$ : Clearance of worker movement in a work cell (mm)

Two auxiliary equipment are considered in a robot work cell layout comprise of robot tooling and work piece. Afterward, a new equation of safety robot workspace area,  $A_w$  for the multiple robot work cell have been derived from the equation (1) as in Figure 2.

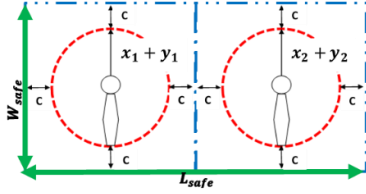


Figure 2 Illustration of safe multiple robot work cell.

$$A_w = L_{safe} \times W_{safe} \quad (2)$$

Where;

$$L_{safe} = \max L \quad (3)$$

$$W_{safe} = \max W \quad (4)$$

$$L = \sum_i^n [2((x_i + y_i) + \dots + (x_n + y_n) + (n \times c))] \quad (5)$$

$$W = \sum_i^n [2((x_i + y_i) + \dots + (x_n + y_n) + (n \times c))] \quad (6)$$

$$L_{safe} = \max \sum_i^n [2((x_i + y_i) + \dots + (x_n + y_n) + (n \times c))] \quad (7)$$

$$W_{safe} = \max \sum_i^n [2((x_i + y_i) + \dots + (x_n + y_n) + (n \times c))] \quad (8)$$

$$1 \leq i \leq \infty \text{ and } 1 \leq n \leq \infty$$

The developed equations involve the safe length in horizontal plane,  $L_{safe}$  and the safe width in vertical plane,  $W_{safe}$ . To provide a reliable solution to this formula, dimension for both  $L_{safe}$  and  $W_{safe}$  must be in the maximum dimension. Subsequently, an optimum robot work cell layout  $L_{opt}$  is determined by selecting the minimum robot workspace area,  $A_w$  of particular robot layout. The equation of the optimum layout can be denoted as:

$$L_{opt} = \min(A_w) \quad (9)$$

### 3.2 Manufacturing throughput time robot work cell

Manufacturing throughput time,  $T_m$  is the total time to convert raw materials into finished products where four categories of time were encompassed [6]:

1. Process time (sec),  $t_p$ : Time taken when work is being done on the product.
2. Inspection time (sec),  $t_i$ : Time taken to check the product is not defective.
3. Move time (sec),  $t_m$ : Time taken to move partially completed or finished products from one workstation to another.
4. Queue time (sec),  $t_q$ : Time taken to wait the product to be worked on, inspected, or moved.

The basic equation for calculating the manufacturing throughput time,  $T_m$  are given below:

$$T_m = t_p + t_i + t_m + t_q \quad (10)$$

Subsequently, new manufacturing throughput time,  $MTT$  equation is modelled based on Figure 3 through

the summation of the robot cycle time,  $RCT$  in the horizontal and vertical manufacturing line cycle time,  $LCT_H$  &  $LCT_V$  where both of  $LCT$  must be the maximum dimension. For the  $LCT_V$ , the first horizontal line is excluded.

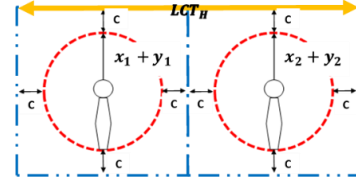


Figure 3 Illustration of manufacturing throughput time for multiple robot work cell.

Due to that, the equations can be expressed as;

$$MTT = \sum_i^n (RCT)_n + \sum_i^n (RCT)_n \quad (11)$$

Where;

$$MTT = LCT_H + LCT_V \quad (12)$$

$$LCT_H = LCT_V = \sum_i^n (RCT)_n \quad (13)$$

$$RCT = T_m \quad (14)$$

For selecting the optimum layout, an equation is proposed as below:

$$L_{opt} = \min(MTT) \quad (15)$$

## 4. CONCLUSIONS

The fundamental concept with the mathematical model for both robot workspace and manufacturing throughput time have been developed. Based on the current outcomes, the robot work cell with minimum workspace area and manufacturing throughput time will be selected to be the optimum layout,  $L_{opt}$  due to it can reduce the use of workspace and manufacturing time within manufacturing line. The developed mathematical equation can be used for the future research in developing computer-based configuration system.

## REFERENCES

- [1] X. Su, "A novel multi-robot workcells designing and positioning method in three-dimensional space," *Int. J. Adv. Comput. Technol.*, vol. 4, no. 19, pp. 1–9, 2012.
- [2] M.A.A. Rahman, "Executable framework for reconfigurable flexible manufacturing system," RMIT University, 2014.
- [3] S. Pellegrinelli, N. Pedrocchi, L. Molinari Tosatti, A. Fischer, and T. Tolio, "Multi-robot spot-welding cells: An integrated approach to cell design and motion planning," *CIRP Ann. - Manuf. Technol.*, vol.63, no.1, pp. 17–20, 2014.
- [4] M.A.A. Rahman, N.S. Osman, C.H. Boon, G.L.T. Poh, A.A.A. Rahman, B.M.B. Mohamad, S.H. Kamsani, E. Mohamad, Z.A. Zaini, M.F.A. Rahman, "Configuring safe industrial robot work cell in manufacturing industry," *J. Adv. Manuf. Technol.*, vol. 10, no. 2, 2016.
- [5] M.A.A. Rahman, "Improvement of Safety system installation for industrial robot work cell," Universiti Tenaga Nasional, 2005.
- [6] C. Drury, *Management and cost accounting*. 2013.

# Optimization of drilling parameters in diameter accuracy on dry drilling process of AISI D2 tool steel

M.H. Osman<sup>1,\*</sup>, M. Hadzley<sup>2</sup>, N.F. Tamin<sup>1</sup>, N.J. Mohamad<sup>1</sup>, M.K. Wahid<sup>1</sup>, M.N. Ahmad<sup>1</sup>, N.A. Maidin<sup>1</sup>,  
M.H. Ab Rahman<sup>1</sup>

<sup>1)</sup> Faculty of Engineering Technology, Universiti Teknikal Malaysia Melaka,  
Hang Tuah Jaya, 76100 Durian Tunggal, Melaka, Malaysia

<sup>2)</sup> Faculty of Manufacturing Engineering, Universiti Teknikal Malaysia Melaka,  
Hang Tuah Jaya, 76100 Durian Tunggal, Melaka, Malaysia

\*Corresponding e-mail: hairizal@utem.edu.my

**Keywords:** Diameter accuracy; AISI D2; tool steel; Taguchi methods

**ABSTRACT** – This paper focuses on the effect of High Speed Steel (HSS) coated drilling tools (TiN, TiCN and TiAlN) and parameters during dry drilling of AISI D2. Taguchi method and ANOVA were used to determine the optimum machining parameter and significant factor that affect the performance of holes' accuracy. The selected parameters were 482- 627 RPM spindle speeds and 68 mm/min -146 mm/min feed rates. The results show that the optimum parameter recorded by using TiCN coated HSS coated with spindle speed at 627 RPM and 103 mm/min feed rate. The drill bit coating type have mainly affects the diameter accuracy based on the highest percentage distribution, followed by the feed rate and spindle speed.

## 1. INTRODUCTION

Drilling is a material removal process to produce cylindrical hole inside the workpiece material. The process started with the used of drill tool that have special design to shear the metal by rotating and evacuating the chip until it penetrated to the required depth. Drilling process normally applied to form the holes for component assembly. In normal application, the material can be drilled according to the diameter of drill tool before assembly process. If the diameter is tight, the operator had to push or squeeze the assembly by applying external force to fit the component of assembly. On the other hand, if the diameter is loose, supporting brackets, gaskets or screws could be applied to tighten the assembly.

Such practice however is not preferable in high end application. For instance, in mold and die industry, drilling process applied to produce many holes for upper and lower die holder. Over tighten or loose diameter accuracy of drill holes may increase the risks of misalignment and fatigue failure as in long term period.

Among many materials that applied as die, AISI D2 is one the most frequently used. AISI D2 Tool Steel possess have high strength and hardness in the range of 54-62 HRC make it very difficult to drill especially when the cutting conditions not applied correctly. Drilling AISI D2 may affect the hole's diameter accuracy due to the formation of low residual stresses around the holes opening and causes the work piece to become more

susceptible to corrosion and crack propagation at the stressed surface [1-2].

There are many previous works study about the process parameters on the diameter accuracy in dry drilling process [1-4]. However, the study focused on the effect of parameters in drilling AISI D2 tool steel is very limited. This paper will be presented the preliminary study on the effect of feed rates, spindle speeds and types of coated drill bit during drilling AISI D2 steel. Taguchi method was used to determine the optimum conditions while ANOVA used to identify significant factors that produce most accurate of holes' diameter in drilling AISI D2 steel.

## 2. METHODOLOGY

The experiments were carried out on 3 axis CNC milling machine in dry condition as shown in Figure 1. AISI D2 tool steel was selected with dimension of 200 mm width × 200 mm length × 13mm thickness size. The machining program has been done using Catia V5 software.

Types of Design of Experiment (DOE) selected in this experiment using Taguchi method. 3 level of study selected as shown in Table 1.

Table 1: The parameter at three levels and three factors.

Factors	Unit	Levels		
		1	2	3
A Feed rate	mm/min	68	103	146
B Spindle rate	RPM	482	550	627
C Drilling tools	11 mm diameter	HSS+TiN	HSS+TiCN	HSS+TiAlN

## 3. RESULTS AND DISCUSSION

Figure 1 shows the main effect plots for diameter accuracy in S/N Ratio. By referring to the Figure 1, the highest value plotted for feed rate is level 2 (103 mm/min). The highest value plotted for spindle speed is from level 3 (627 RPM) while for drill bit types is contributed by level 2 (HSS coating with TiCN). The highest value in SN ratio graph shows the optimum parameter needed. This is because the higher values of

SN ratio identify control factor settings that minimize the effect of the noise factors which is lower the effect of noise factor. There is no horizontal line plotted. Hence, it shows that the combination of higher level of feed rate, spindle speed and drill bit coating can give the minimum S/N Ratio among the all possible combinations.

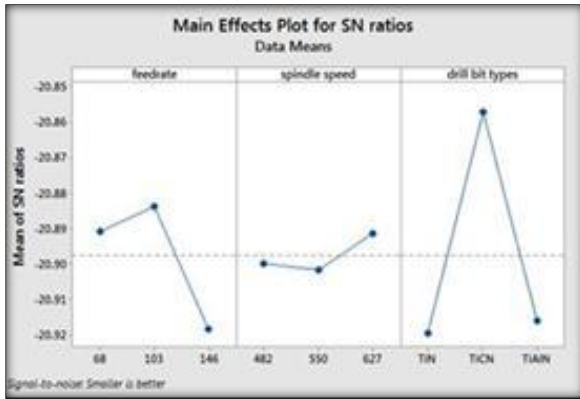


Figure 1 Main effect plots for SN ratios.

Figure 2 shows the main effects plot on diameter accuracy based on the means value. By referring to Figure 2, the lowest value plotted for feed rate is from level 2 (103 mm/min). The lowest value plotted for spindle speed is from level 3 (627 RPM) while for drill bit types is contributed by level 2 (HSS coating with TiCN). Therefore, the optimum parameter suggested by Taguchi is the combination of A2B3C2 (103 mm/min), (627 RPM), (HSS coating with TiCN) which give the most accurate diameter.

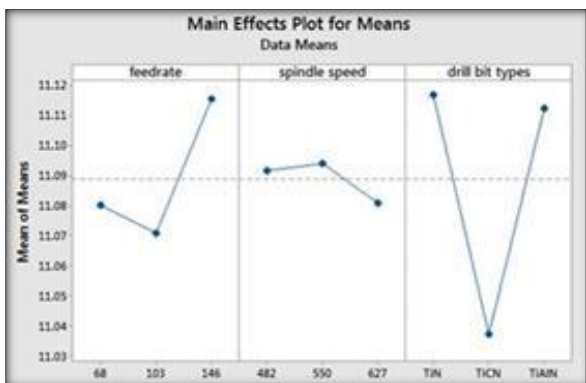


Figure 2 Main effect plots for means.

Table 3 shows the result of ANOVA. Through the Table 3, the P-value of coating types is 0.043 which is less than 0.05 corresponding to 95% confidence level. It indicates that this factor has significant contribution on the diameter accuracy. This factor also possesses the highest percentage contribution which is 74.32%. This is followed by feed rate 20.46% and spindle speed 1.86%. It should be noted that percentage of contribution for feed rate and spindle speed are too small, reflected that these factors not contributed so much to the diameter accuracy.

Based on Table 3, the coating types of drilling tools appeared at first rank which mean it is the most significant factor. Narendraprasad [4] stated that multi abrasive coating material will increase lubricant while reducing the friction as well as temperature generation.

As cutting tool shear the material with lower temperature, the stability of cutting tool can be retain for longer period of time. Thus, it results more accurate of material removal process that produces better accuracy of holes' diameter. In this case, the using of high speed steel (HSS) with TiCN coating contribute most accuracy. Titanium Carbon Nitride (TiCN) is an abrasion resistant ceramic coating that formed by addition of small amount of carbon to the Titanium Nitride (TiN) during the deposition process. This coating is harder than TiN which provides the cutting edge with good protection from wear.

Table 3: ANOVA Results of Analysis

Source	D F	Adj SS	F	P	% of Cont.
Feed R	2	0.0032	6.14	0.140	20.4
Spindle S	2	0.0003	0.56	0.641	1.86
Drill Bit Coating T	2	0.0119	22.28	0.043	74.3
R error	2	0.0005			3.1
Total	8	0.0161			100

#### 4. CONCLUSIONS

There are several conclusions can be made based on the results:

1. The optimum parameter is observed by using HSS coated with TiCN while the feed rate at 103 mm/min and spindle speed at 627 RPM.
2. The drill bit coating type have mainly affects the diameter accuracy based on the highest percentage distribution, followed by the feed rate and spindle speed.

#### ACKNOWLEDGEMENT

Authors are grateful to Universiti Teknikal Malaysia Melaka for the financial support through PJP High Impact Research Grant numbered PJP/2015/FTK(31B)/S01456.

#### REFERENCES

- [1] J.A. Arsecularatne, L.C. Zhang, C. Montross and P.Mathew, "On machining of hardened AISI D2 Steel with PCBN tools", *J. of Mat. Processing Tech.*, vol.171, pp. 244-252, 2005
- [2] I. Tekaut , and H. Demir, "The Effects Of Cutting Tool Coating And Machining Parameters In Drilling Of Steel AISI H13 And AISI D2," *J. of the Faculty of Eng. and Architecture*, vol. 30, pp .289-296, 2015
- [3] V. Derflinger, H. Brandle, and H. Zimmermann, "New hard lubricant coating for dry machining," *J. of Surface and Coatings Tech.*, vol.113, pp. 286-292, 1999
- [4] V. Narendraprasad, "Experimental Investigation of Coating on High Speed Steel Cutting Tool", *Int. J. of Inn Research in Tech, Science & Eng*, vol.1, 2015.

# The correlation between S11 and S21 techniques measured in a network analyzer from 45MHz until 50GHz

Ming Hui Tan<sup>1</sup>, Ahmad Yusairi Bani Hashim<sup>2</sup>, Mohd Rizal Salleh<sup>2</sup>

<sup>1</sup>) Radio Frequency Calibration Laboratory, National Instruments Malaysia Sdn Bhd, Malaysia

<sup>2</sup>) Faculty of Manufacturing Engineering, Universiti Teknikal Malaysia Melaka, Hang Tuah Jaya, 76100 Durian Tunggal, Melaka, Malaysia

\*Corresponding e-mail: ming.hui.tan@ni.com

**Keywords:** Calibration; network analyzer

**ABSTRACT** – This paper is an analysis and study regarding the Radio Frequency (RF) connector insertion loss in applications at 50-ohm impedance from 45MHz until 50GHz by using the Network Analyzer and two type of techniques that are reflection one port (S11) and full two port (S21) insertion loss calibration. RF connector will always assume as lossless in a RF calibration system. It can exist in varying types in dimension and length that is called delay line. The objective is to gain more knowledge about the two types of calibration techniques by using the mechanical and electronic calibration kits. The purpose of this study is using the S11 and S21 techniques to measure the RF connector loss against its frequency range and analyze the differences between both techniques to determine which technique is more precise and accurate.

## 1. INTRODUCTION

RF connectors are found in a broad range of electronic equipment for extending the dynamic range of measuring equipment. Characterizing RF connector requires an accurate attenuation measurement such as Network Analyzer. As previous study [1] the HP8510 was choose to perform the calibration while this study is using the E8364B. RF connector can be found in many dimensions and its operating frequency range. The problem is RF connector itself having insertion loss. It has voltage drop when a signal pass thru the RF connector. RF connector does not require annual calibration because it will be an exorbitant calibration cost. However, if a fragmented RF connector had been connected to the RF test system, it will possible to break down the entire system. Another common solution that is keeping the safety stock for RF connectors. However, it is not practicable because it will increase the entire operating cost and impact the return on revenue ratio. This study will show the different between S11 and S21 techniques in a network analyzer and determine the port match of the RF connector. At the end of the study will implement an excel spreadsheet to calculate the Linear Magnitude (Lin Mag), loss in dB and degree from the “real and imaginary (.cti)” format in the Network Analyzer after the RF connector had been measured its losses.

## 2. METHODOLOGY

This study will provide a possible solution on how

to measure an unknown RF connector shows in Figure 1. As previous study [2] explains why use S-parameter to characterize the high frequency networks.

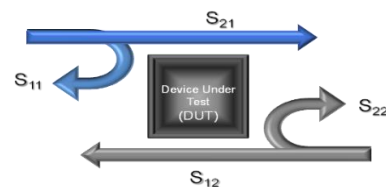


Figure 1 S-parameter measured with a device.

This paper will study how to create a system that can calibrate all of the RF connector by using S11 and S21 method on a 2.4mm RF connector as previous study [3] can operate until 60GHz. Figure 2 shows the overall process require to perform the RF connector insertion loss.

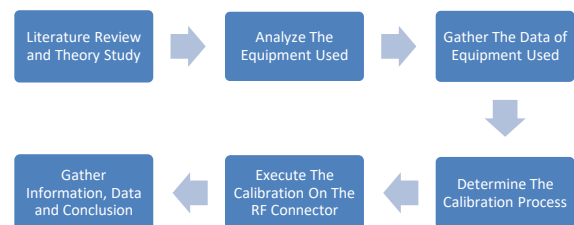


Figure 2 A flow chart to calibrate RF connector.

S11 calibration is only consists of single port calibration in a network analyzer either in S11 or S22 shown in Figure 3. It is the simpler method to perform the calibration without any specific or high skills. After the S11 or calibration complete, connect the RF connector at the open port of the network analyzer and terminate with the calibration kits “Short”. The usage and purpose of the calibration kits “Short” is perform a full reflected voltage back to the network analyzer. The network analyzer will measure the loss (voltage drop) across the RF connector. It is also known as port match. However, in this method the port match will define as insertion loss of the RF connector measured.

S21 is a technique that require to perform a full two ports calibration in the network analyzer. It is consisting both port 1 and 2 in the network analyzer. RF connector will apply in between port 1 and 2 in the network analyzer



shown in Figure 2. The voltage drops from port 2 to port 1 will measure as RF connector loss. Besides that, this method will measure all the 4 parameters. It is S11, S12, S21 and S22. This method required high skills and consume a lot of time to calibrate it.



Figure 3 S11 one port calibration (left) and S21 full two ports calibration (right).

### 3. RESULTS AND DISCUSSION

After the calibration completed, the measurement results required to store in real and imaginary. Save the RF connector S-parameter file under “real and imaginary (.cti)” format from the network analyzer. This data can be re-opened in Microsoft Excel and applying some mathematic model towards the .cti file. It is to recalculate the insertion loss in the excel worksheet shown in Equation 1, 2 and 3 respectively.

Equation 1 Real and Imaginary convert to Lin. Mag.

$$Lin\ Mag = (\sqrt{Real^2 + Imag^2}) \quad (1)$$

Equation 2 Conversion for Lin. Mag. to loss in dB

$$Loss\ in\ dB = (20\ Log\ \sqrt{Real^2 + Imag^2}) \quad (2)$$

Equation 3 Conversion for real and imaginary into degree

$$Degree = \left( \tan^{-1} \frac{Imag}{Real} \times \frac{180}{\pi} \right) \quad (3)$$

Once the conversion is complete calculated in excel worksheet, plot the data accordingly. Refer to Figure 3, blue and or red line represent mechanical calibration kits performed for S11 parameter M Cal S1p (blue line) and S21 parameter M Cal F2p (red line). The green and orange line represent electronic calibration kits performed for S11 parameter Ecal S1p (green line) and S21 parameter Ecal F2p (orange line).

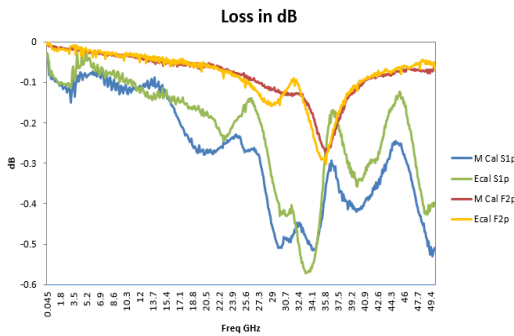


Figure 4 The differences for single one port S11 and full two port S21 measured by using mechanical and electronic calibration kits.

From the Figure 4, it shows that M Cal F2p and Ecal F2p measure the lowest loss for RF connector. Both

method is S21 full two ports calibration measure more accurately compares to S11 single one port (S1p).

Figure 5 shows the port match difference between mechanical and electronic calibration kits in S21 full two ports calibration. For the port match calibration, it is known that the lower dB measure in network analyzer the better performance it is. The results gather in Figure 5 shows that mechanical calibration kits measure very well in port 1 (M Cal S11). It is the lowest voltage reflection coefficient for the entire frequency range up to 50GHz. While electronic calibration kits at port 2 of the network analyzer measure the highest voltage reflection coefficient at approximate 36.5GHz.

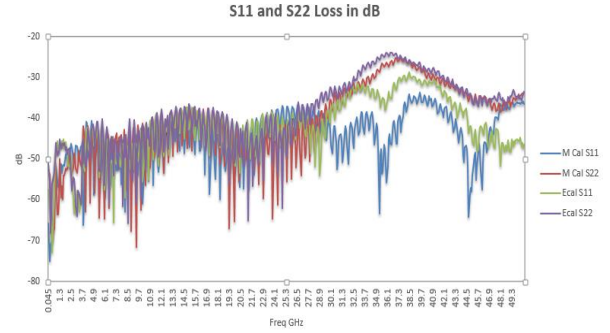


Figure 5 The differences of the port match between S11 and S22 measured by mechanical and electronic full two port calibration.

### 4. CONCLUSIONS

Conclude that this study guides the operation of a network analyzer and calibration kits to perform the calibration according to the standards procedures. Calibration Kits are well establishing to evaluate the technique of ports calibration. The S1p and F2p techniques also successful measured in this paper by using mechanical and electronic calibration kits. It is a unique process to calibrate a RF connector measured from 45MHz until 50GHz. Once the insertion loss of the RF connector had been determined, the loss of the RF connector can be compensated in the RF tester in production. In this paper, the worst case of the insertion loss had been measured is approximate -0.6dB. However as previous study [4] found that that are a few techniques to determine the in-tolerance or out-of-tolerance between all 4 techniques correlation. From Figure 4 it can justify that M Cal F2p and Ecal F2p were found in-tolerance while another two techniques were found out-of-tolerance.

### REFERENCES

- [1] P. Pino, Intermateability of SMA, 3.5-mm, and 2.92-mm Connectors, Newark, Delaware: W. L. Gore & Associates, Inc, January 2007.
- [2] Agilent Network Analyzer Basics, USA: Agilent Technologies 5965-7917E, August 31, 2004.
- [3] D. Skinner, Guidance on using Precision Coaxial Connectors in Measurement (3rd Edition), UK: National Physical Laboratory, August 2007.
- [4] M. Dobbett, Understanding Measurement Risk, USA: Agilent Technologies, 2012.

# Development of fixable rotation clamping method for milling machine

N.B. Ab Wahab<sup>1,2,\*</sup>, M.H. Abdul Rani<sup>1</sup>, A.K. Nordin<sup>1</sup>, N.F. Tamin<sup>1</sup>, A.A. Onn<sup>1</sup>

<sup>1</sup> Faculty of Engineering Technology, Universiti Teknikal Malaysia Melaka,  
Hang Tuah Jaya, 76100 Durian Tunggal, Melaka, Malaysia

<sup>2</sup> Advanced Manufacturing Center, Universiti Teknikal Malaysia Melaka,  
Hang Tuah Jaya, 76100 Durian Tunggal, Melaka, Malaysia

\*Corresponding e-mail: norfariza@utem.edu.my

**Keywords:** Fixable rotation; clamping; milling

**ABSTRACT** – Clamping or work holding is a generic term for any device used to hold the workpiece during machining process. However, only limited surface of the workpiece can be cut in a single clamping. The objective of this project, is to design, develop and evaluate fixable rotation clamping method for milling process. After the device was developed, one testing was done on the fixable rotation clamping to evaluate the product output parameter which was surface roughness. The results indicate that the average of surface roughness value using current vise as a clamping method is higher than using the newly developed clamping. This shows promising results for the new device.

## 1. INTRODUCTION

Milling process is one of the most important processes in manufacturing process which can make an assortment of elements on a material by removing the unwanted material. Thus, the milling process requires a milling machine, work-piece, fixture and cutter. There are many types of milling machine with different function and characteristic which is universal horizontal milling machine, ram-type milling machine, universal ram-type milling machine, knee-type milling machine, and swivel cutter head ram-type milling machine.

Material will be removed from the work-piece by sustaining the work-piece into the rotating cutter as little chips to make the wanted shape. This makes the manufacturing environment becoming more competitive. To overcome these diverse issues, its needed technology support in improving the flexibility and automation to improve the manufacturing environment as a main reason for the introduction of Flexible Manufacturing Systems [1]. While, the operations that often used by a manufacturer in a milling machine is face milling, end milling, slotting, thread milling, plain milling and side milling [2].

The primary function of a clamping vise is to position and fix the workpiece. Once placed, the workpiece should even be control to stop movement throughout the process.

## 2. METHODOLOGY

This study was conducted as shown in Figure 1. It been divided into three stage. The stages were:

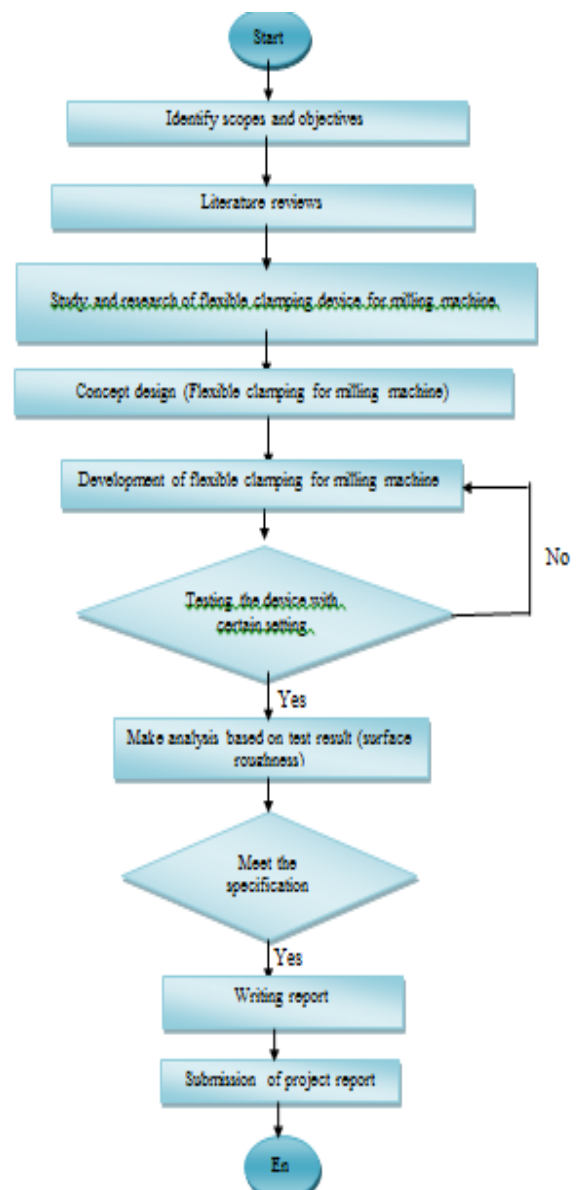


Figure 1 Flow chart of this research.

### 2.1 Design of fixable rotation clamping

In this stage, since the problem statement was well defined and all the variables related to the study are well established, the idea of product design was sketched.

Next, a sketch of the product is drawn to solve the problem statement. Then, the sketch is redrawing by using CATIA software. Figure 2 shows the final expected product to be process.

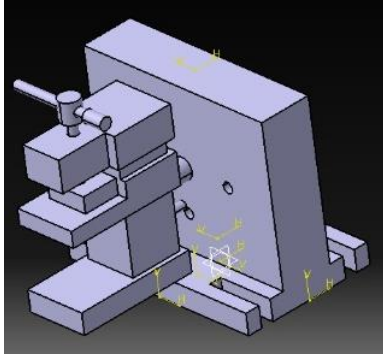


Figure 2 Design of flexible clamping using CATIA software.

### 2.2 Development of fixable rotation clamping

All the machining process totally use by conventional machine that available in the laboratory only such as milling machine, drilling machine and turning machine. Total part to be develop is 8 parts.

### 2.3 Surface roughness tetsting

After the product is complete, the product will be tested on milling machine with certain parameters to compare with current vise which is using same setting parameters.

The comparison was made based on the surface roughness of the work piece between using both clamping method.

Two types of material were used in this testing which is aluminium.

### 2.4 Experimental setup

Developed fixable rotation clamping device had been setup for test as shown in Figure 3.



Figure 3 Experiment setup to evaluate the developed device.

## 3. RESULTS AND DISCUSSION

Table 1 shown that the average of Ra value using current vise as a clamping method is higher than using fixable rotation clamping as a clamping method which are 1.543 when using current vise and 1.151 when using fixable rotation clamping. This proves that fixable rotation clamping can be used as a clamping method due to its surface finish is better than using current vise.

Table 1 Result of surface roughness on aluminium workpiece.

Reading	Ra value using current vise	Ra value using flexible clamping
1	1.484	0.639
2	1.469	1.958
3	1.764	0.599
4	1.431	1.097
5	1.739	1.194
6	1.737	1.323
7	1.410	0.980
8	1.495	1.244
9	1.418	1.278
10	1.481	1.194
<b>Average</b>	<b>1.543</b>	<b>1.151</b>

## 4. CONCLUSIONS

As conclusion, this project was developed to overcome the problem when using current vise at milling machine which is there are limited surface can be cut in one single clamp. This fixable rotation clamping is able to rotate 90 degree for both sides. So, all surfaces of the work piece can be cut in one single clamp. As all the three of the objectives was achieved which means that the flexible clamping for milling machine was designed and developed. Besides, the results of surface roughness also were evaluated by using this developed clamping device. However, when using aluminum as a work piece, the Ra value using current vise is lower than flexible clamping. This proves that the rigidity of flexible clamping is not good for hard material compared to soft material such as delrin.

## REFERENCES

- [1] M. Nurdin, A.L. Hakim, "A development of flexible manufacturing system using POLMAN T-100 vise casting component as a case study," *Procedia Manufacturing*, vol. 2, pp. 77–81, 2015.
- [2] D. Vukelic, B. Tadic, D. Miljanic, I. Budak, P.M. Todorovic, S. Randjelovic, "Novel workpiece clamping method for increased machining performance," *Tehnički Vjesnik*, vol. 19, pp. 837–846, 2012.

# Earth tubes for assisting passive cooling in Masjid Sayyidina Abu Bakar, UTeM

S.N. Khalil<sup>1,2\*</sup>, N.N. Hamzah<sup>1</sup>

<sup>1</sup>) Faculty of Mechanical Engineering, Universiti Teknikal Malaysia Melaka, Hang Tuah Jaya, 76100 Durian Tunggal, Melaka, Malaysia.

<sup>2</sup>) Centre for Advanced Research on Energy, Universiti Teknikal Malaysia Melaka, Hang Tuah Jaya, 76100 Durian Tunggal, Melaka, Malaysia.

\*Corresponding e-mail: snurhaidakhalil@utem.edu.my

**Keywords:** Passive cooling; thermal comfort; energy sustainability

**ABSTRACT** – Passive cooling is a cooling system that focuses on the works of heat gain control and also dissipation or release of heat in order to improve the indoor thermal condition with low or no energy consumption. It prevents heat from entering the interior of the building or removing heat from the building known as natural cooling. Passive cooling are normally has no use of the typical mechanical devices such as fans and air conditioners. Passive cooling are normally related to natural cooling where it uses the nature such as trees and its natural surroundings to cool down the nearby buildings. Design of the building itself can also contribute to passive cooling of the building. This type of cooling is deemed as the best way to reduce the electrical energy consumption especially in the hot and humid equatorial climate where 40 percent of the world population are currently staying. Masjid Saiyyidina Abu Bakar which is situated in the main campus of Universiti Teknikal Malaysia Melaka is chosen as the case study in this research. This research will explain on how the passive cooling improves thermal comfort in the building. The proposed solution for this is the installation of earth tubes to improve the cross ventilation in the building. Simulation of this passive cooling method has been performed and the result is discussed in this paper.

## 1. INTRODUCTION

The main purpose of this research is to design solutions to assist the passive cooling in Masjid Sayyidina Abu Bakar. Masjid Saiyyidina Abu Bakar is located in the main campus of Universiti Teknikal Malaysia Melaka in Durian Tunggal, Melaka. Masjid Sayyidina Abu Bakar is a three-storey building. This is a religious multifunction building for the Muslims with a capacity of 4000 congregation [1]. This masjid may have influenced by the traditional local architecture that follows the design of Malay traditional house marked by the roof geometry of a pyramidal [2]. This masjid distributed into two prayer hall with approximate volume of 19500 meter cube [1]. The main prayer hall that is located on the second floor has total area of 1200 meter square [1]. While the second prayer hall, which is the women prayer hall that is located on the third floor has a smaller area of 560 meter square [1]. With large spaces, it is hard to achieve comfortable thermal condition especially during prayer times i.e. Friday prayer

congregation [3]. To keep up with the amount of member of congregations, the active cooling method is often used i.e. via mechanical devices such as fans and air conditioning, however this will cost a lot on the energy bill. In regards to this the researcher is proposing passive cooling method to improve thermal comfort within the masjid without incurring any cost to the energy bills, in support of energy management and energy sustainability efforts in UTeM.

## 2. METHODOLOGY

The research was held by conducting literature review on the broad subject of passive cooling, geological location factor and architectural designs on mosques in Malaysia and narrowed down to passive cooling design which is available in the market. This design is then proposed for Masjid Saiyyidina Abu Bakar to improve its thermal comfort. The design solution and its analysis via computer simulation is discussed in this paper.

## 3. RESULTS AND DISCUSSION

The temperature readings taken during daylight, the data shows that the peak temperature is between at 11am to 2pm. (refer Figure 1). The temperature was taken at the positions labelled in Figure 2:

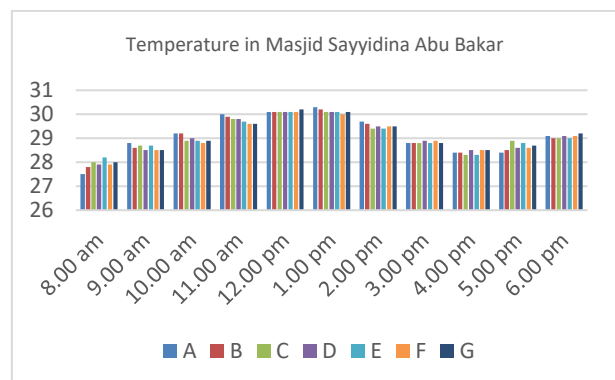


Figure 1 Temperature profile of Masjid Sayyidina Abu Bakar UTeM.

Based on this data, the researcher proposed solution i.e. installation of earth tubes in the building of the masjid to improve cross ventilation in the masjid. This proposed



solution is chosen due to the suitability of its application on an existing building.

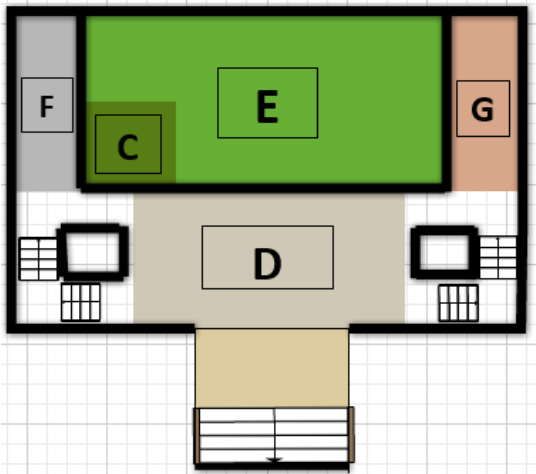


Figure 2 Floor plan of the first floor and area markings.

As stated in design consideration, the tubes are made of polyvinylchloride (PVC) due to its cost, resistance to corrosion, and easy to apply. The tubes are connected from the chimney (Figure 3) to the underground tubes and also from the underground tubes to the targeted rooms. Tubes within the targeted room i.e. the main prayer hall are placed slightly above the doors. The diameter of these tubes are 0.2m to comply with the diameter of the chimney and design considerations. The proposed design is as follows in Figure 4 and 5. Pressure difference between hot air (from the building) and cold air (outdoor) creates draught, thus improves air movement and induce better cross ventilation.



Figure 3 Air trap chimney.

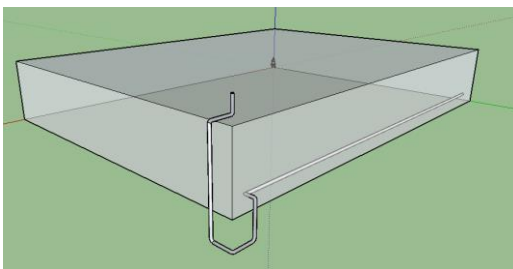


Figure 4 System overview.

This design has been simulated in EnergyPlus i.e. an open source software that provides Energy Management System (EMS) feature that support and provide custom control and modeling for buildings and houses. It is designed as a tool to simulate energy and load in a building etc.

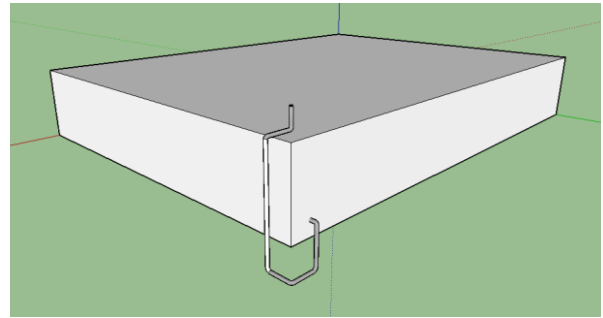


Figure 5 System from the outside.

The results from the simulation of the application of earth tubes to the masjid building is as referred as follows in Figure 6. The output temperature from the earth tubes in the building is lower than masjid and outdoor temperature, thus improve thermal load in the building.

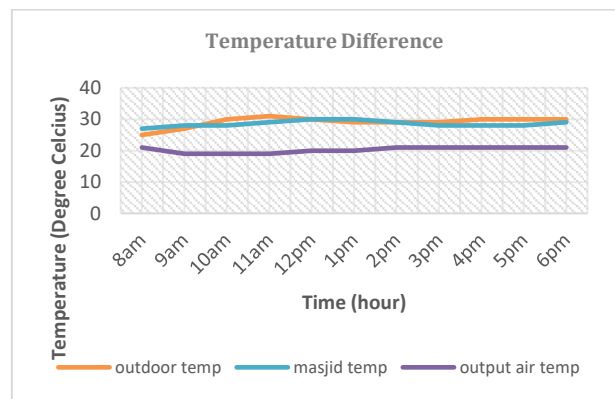


Figure 6 Simulation results of earth tubes application in masjid.

#### 4. CONCLUSIONS

From the design and analysis, it can be concluded that passive cooling via the application earth tubes is promising as the temperature in masjid can be reduced by approximately 20%. Therefore, it can be further investigated via prototype development and experimental testing.

#### REFERENCES

- [1] D. Kassim, A. Putra, M.J.M. Nor, "The acoustical characteristics of the Sayyidina Abu Bakar, UTeM," *Journal of Engineering Science and Technology*, vol. 10, no. 1, pp. 97-110, 2015.
- [2] M.T.M. Rasdi, "Mosque architecture in Malaysia: Classification of styles and possible influence", *Jurnal Alam Bina*, vol. 9, no. 3, pp. 1-37, 2007.
- [3] A. Ali, "Passive cooling and vernacularism in Mughal buildings in North India: a source of inspiration for sustainable development," *International Transaction Journal of Engineering, Management and Applied Science and Technology*, vol 4, no. 1, pp. 15-27, 2012.

# Geometrical shrinkage comparison between gate direction and transverse direction of plastic part in plastic injection molding

M.A.M. Amran\*, N. Idayu, S. Sivarao, M.S. Salleh, Z. Abdullah

Faculty of Manufacturing Engineering, Universiti Teknikal Malaysia Melaka,  
Hang Tuah Jaya, 76100 Durian Tunggal, Melaka, Malaysia

\*Corresponding e-mail: mohdamran@utem.edu.my

**Keywords:** Shrinkage direction; Taguchi method

**ABSTRACT** – In this paper, the main objective is to determine the shrinkage for gate and transverse direction of plastic part. Taguchi method was selected as the design of the experiment by considering mould temperature, melt temperature, injection time and cooling time as process variables. It was found that higher shrinkage happened in the gate direction compared to transverse direction and mould temperature was the most significant parameter that affected the shrinkage for both directions.

## 1. INTRODUCTION

Shrinkage at gate and transverse direction was the most affected geometrical value in plastic assembly process. This phenomenon happens due to the unoptimized of process condition. Therefore, several researchers evaluated the influence of process conditions of injection molded parts on shrinkage [1]. Annicchiarico et al. [2] studied the shrinkage of micro moulded part by considering the shrinkage parallel and normal to the flow. They found that mould temperature was the most influenced factor for the shrinkage in both flow direction. Therefore, the aim of this paper is to determine the shrinkage for gate and transverse direction of plastic part and the most influence parameter that affect the shrinkage.

## 2. METHODOLOGY

The parameters used for the experiment analyses were the mould temperature (MoT), melt temperature (MeT), injection time (IT) and cooling time (CT). Taguchi method with an orthogonal table of  $L_9 (3^4)$  that has four factors and three levels was implemented from our previous paper [3] and presented in Table 1. The plastic material, polypropylene (PP) was used for experiment, supplied by Lotte Chemical Titan (M) Sdn. Bhd. The melt mass-flow rate of material was 4 g/10 min and has density of 0.9 g/cm<sup>3</sup>. In addition, the injection molding used for the experiment was Allrounder 370 H 600-170 Hybrid machine (Arburg).

Table 1 Process parameters of the experiment.

Process Parameters	MoT (°C)	MeT (°C)	IT (s)	CT (s)
Low	50	250	0.63	12.6
Medium	56	280	0.70	14.0
High	62	310	0.77	15.4

## 2.1 Shrinkage test

For the shrinkage calculation, Rahimi et al. [4] used a digital caliper to determine the shrinkage of the plastic specimen. So, the shrinkage was performed using digital caliper with the precision of 0.01 mm.

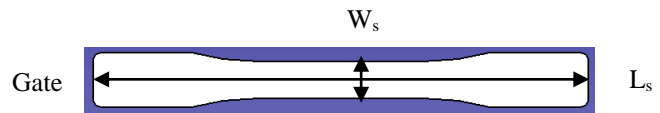


Figure 1 Shrinkage direction of plastic part.

Measurement of length of specimen in gate direction is  $L_s$  while the measurement of width of specimen in transverse direction is  $W_s$  as shown in Figure 1. The shrinkage was calculated using the following equations (1) and (2) given below.

Shrinkage in gate direction,  $S_G$

$$S_G = \frac{(L_m - L_s)}{L_m} \times 100 \quad (1)$$

Shrinkage in transverse direction,  $S_T$

$$S_T = \frac{(W_m - W_s)}{W_m} \times 100 \quad (2)$$

Where  $L_m$  and  $W_m$  are the length and width of the mold respectively.

## 3. RESULTS AND DISCUSSION

### 3.1 Shrinkage measurement results

Table 2 shows the Taguchi orthogonal array with total 9 runs and the shrinkage result for gate and transverse direction of plastic part.

Table 2 Total shrinkage of ( $S_G$ ) and ( $S_T$ ) for plastic part.

Run	MoT (°C)	MeT (°C)	IT (s)	CT (s)	$S_G$ (%)	$S_T$ (%)
1	50	250	0.63	12.6	1.73	1.11
2	50	280	0.70	14.0	1.76	1.10
3	50	310	0.77	15.4	1.72	1.07
4	56	250	0.70	15.4	1.73	1.14
5	56	280	0.77	12.6	1.77	1.13
6	56	310	0.63	14.0	1.82	1.15
7	62	250	0.77	14.0	1.80	1.22
8	62	280	0.63	15.4	1.84	1.19
9	62	310	0.70	12.6	1.86	1.19

From the experiment result, higher shrinkage was found in the gate direction compared to transverse direction. This is called as the characteristic of semicrystalline polymers such as PP due to the phase changes from amorphous to crystalline. It is also related to the volume reduction process during cooling stage. Moreover, during the injection stage, the polymeric long chains will orient or align in flow (gate) direction. Once in the mold cavity, outer layers of polymer are cooled faster than inner layers that allows the inner layers more time to relax and disorient or misalign[1, 5].

### 3.2 Taguchi analysis for optimal process variables

In Figure 2, S/N ratios are plotted for each factor and their levels. By using the data from the experiment, optimal shrinkage was predicted using “Predict Taguchi Result” function in Minitab software. Optimum factor levels for shrinkage in gate direction were mould temperature 50°C, melt temperature 250°C, injection time 0.77s and cooling time 15.4s that has 1.67% of shrinkage. Meanwhile, the optimum parameter levels for transverse shrinkage is the same as run number 3 that has mould temperature 50°C, melt temperature 310°C, injection time 0.77s and cooling time 15.4s.

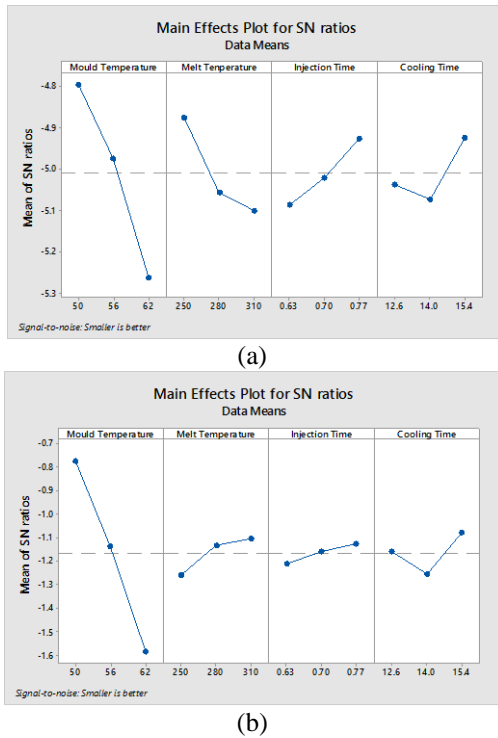


Figure 2 S/N ratios for shrinkage in (a) gate direction, S<sub>G</sub> and (b) transverse direction, S<sub>T</sub>.

### 3.3 ANOVA analysis

ANOVA was performed for both shrinkage direction and from the result as shown in Table 3 to determine the most influential parameter on the quality characteristics. It is found that mould temperature is significant parameter for shrinkage in gate and transverse directions due to the p-values are less than 0.05. In addition, mould temperature also has a great impact on both shrinkage in gate and transverse direction of plastic part due to the highest percentage

contribution, P of 67.76% and 91.15% respectively.

Table 3 ANOVA result.

Parameters	S <sub>G</sub>		S <sub>T</sub>	
	p-value	P (%)	p-value	P (%)
MoT	0.034	67.76	0.001	91.15
MeT	0.568	17.18	0.894	3.66
IT	0.778	8.01	0.975	0.83
CT	0.803	0.803	0.975	4.37
		100		100

According to Annicchiarico et al. [2], shrinkage was reduced upon increasing the crystallinity. In polymer, the temperature parameters such as mould and melt temperature are known to drive the crystal growth or rate of crystallization by controlling the transition from melt to solid state.

## 4. CONCLUSIONS

It can be concluded that shrinkage in the gate direction is higher compared to the transverse direction. In addition, mould temperature also is the most significant parameter that affected shrinkage for both gate and transverse direction.

## ACKNOWLEDGEMENT

Grant no.: RAGS/1/2014/TK01/FKP/B00075.

## REFERENCES

- [1] A. M. Cadena-Perez, I. Yañez-Flores, S. Sanchez-Valdes, O. S. Rodriguez-Fernandez, S. Fernandez-Tavizon, L. F. R. de Valle, T. Lozano-Ramirez, J. G. Martinez-Colunga, and J. L. Sanchez-Cuevas, “Shrinkage reduction and morphological characterization of PP reinforced with glass fiber and nanoclay using functionalized PP as compatibilizer,” *Int. J. Mater. Form.*, vol. 10, no. 2, pp. 233–240, 2017.
- [2] D. Annicchiarico, U. M. Attia, and J. R. Alcock, “A methodology for shrinkage measurement in micro-injection moulding,” *Polym. Test.*, vol. 32, no. 4, pp. 769–777, 2013.
- [3] M. A. M. Amran, N. Idayu, K. M. Faizal, M. Sanusi, R. Izamshah, and M. Shahir, “Part weight verification between simulation and experiment of plastic part in injection moulding process,” in *IOP Conference Series: Materials Science and Engineering*, vol. 160, pp. 1–7, 2016.
- [4] M. Rahimi, M. Esfahanian, and M. Moradi, “Effect of reprocessing on shrinkage and mechanical properties of ABS and investigating the proper blend of virgin and recycled ABS in injection molding,” *J. Mater. Process. Technol.*, vol. 214, pp. 2359–2365, 2014.
- [5] R. Revilla-Díaz, S. Sánchez-Valdés, F. López-Campos, F. J. Medellín-Rodríguez, and M. L. López-Ouintanilla, “Comparative characterization of PP nano- and microcomposites by In-mold shrinkage measurements and structural characteristics,” *Macromol. Mater. Eng.*, vol. 292, no. 6, pp. 762–768, 2007.

# Optimization of mixed-model assembly line balancing problem with resource constraints

M.M. Razali, M.F.F. Ab Rashid\*, M.R.A. Make

Faculty of Mechanical Engineering, Universiti Malaysia Pahang,  
26600 Pekan, Pahang, Malaysia

\*Corresponding e-mail: ffaisae@ump.edu.my

**Keywords:** Mixed-model assembly line balancing; evolutionary algorithm; resource constraints

**ABSTRACT** – In this study, mixed-model assembly line balancing problem is used to analyze the performance of four evolutionary algorithms (EAs), namely particle swarm optimization (PSO), simulated annealing (SA), ant colony optimization (ACO) and genetic algorithm (GA). Three categories of test problem (small, medium, and large) is used ranging from 8 to 100 number of tasks. For computational experiment, MATLAB software is used in investigate the EAs performance to optimize the designated objective functions. The results reveal that ACO performed better in term of solution quality of fitness function. However, in term of processing time, PSO was the fastest followed by ACO, GA, and SA.

## 1. INTRODUCTION

Assembly line balancing problem (ALBP) is a matter of decisions that arise when designing or redesigning the assembly line and it involves finding the optimum assignment of tasks. In the recent decades, ALBP has been one of the major interesting research subjects due to its importance to the manufacturers nowadays. Mixed-model assembly line balancing problem (MMALBP) is categorized under ALBP. It differs with the other problem in ALBP classification because it deals with an assembly line that capable to assemble more than one different product at the same time on the same assembly line [1].

In context of MMALBP, various other factors are considered. As an example, the number of models which will be assembled and total demand throughout planning horizon. There are a few methods that has been used by previous researcher to propose a potent solution for this problem. For instance, they utilize a mathematical approach namely mixed integer linear programming and mathematical programming techniques that aimed to optimized MMALBP [2]. However, problems associated with the use of optimization in large-scale engineering problems frequently reach local optimum especially when facing NP-hard problems.

In order to counter this problem, some alternative solutions are proposed. Researchers have presented an algorithm (the so-called evolutionary algorithm) to find near-optimal solution to the MMALBP. Evolutionary Algorithms (EAs) are stochastic optimizer programming that capable to solve multi-objective optimization problems. They able to deal with the multi-objective problems with a set of possible solutions simultaneously [3]. The algorithms can find the optimal solution in a

single run compared with traditional techniques that need to be execute in a series of separate runs.

This paper investigates on mixed-model assembly line balancing problem and provides computational study of the performance comparison of four stochastic search algorithms in term of solution quality of fitness value and processing time. These four EAs technique inspired by different natural process namely ant colony optimization (ACO), genetic algorithm (GA), particle swarm optimization (PSO), and simulated annealing (SA). Three objectives function are chosen which is minimize total cycle time, minimize product rate variation, and minimize number of resources used on the assembly line.

## 2. METHODOLOGY

In order to evaluate the performance of selected EAs, a modelling was constructed with the objective functions to minimize cycle time, minimize product rate variation (PRV) and resources used on the assembly line, refer [4]. After that, the optimization takes place by applying selected algorithm. Figure 1 illustrated the flow of optimizing the test problem using EAs, for example shown below is by using ACO algorithm.

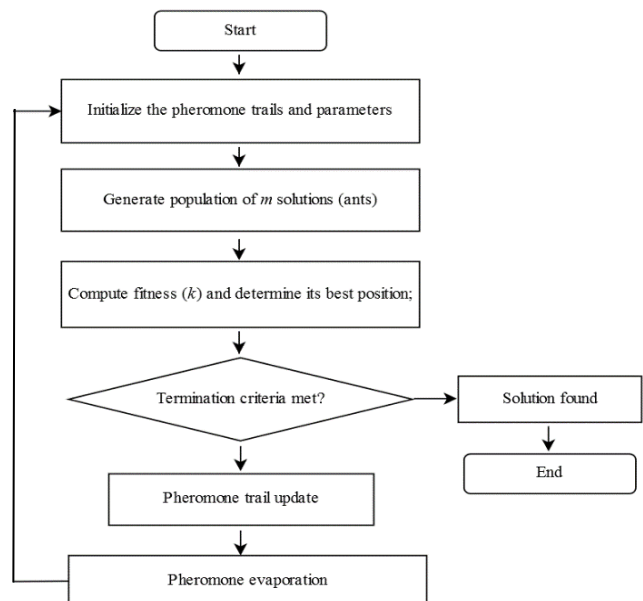


Figure 1 ACO process flow chart.



### 3. RESULTS AND DISCUSSION

In order to evaluate the performance ACO, GA, PSO, SA to extend limit, a large number of dataset must be tested. The test problems used in this paper is taken from the website 'http://www.assembly-line-balancing.de' under the categories of mixed-model assembly line balancing problem. The dataset contains small-size test problem (STP), medium-size test problem (MTP) and large-size test problem (LTP) ranging from 8 to 100 number of tasks. Specifically, small size problem contains 8 tasks to 20 tasks, medium size problem ranges from 25 to 50 tasks and large size problem from 60 to 100 number of tasks. Hence, all aforementioned EAs is being tested by using the chosen test problems. Then statistical analysis is made to test the significance levels ( $\alpha=0.05$ ) for each result returned by the EAs. The result from this comparison of performance is presented as in Table 1-3.

Table 1 EAs computational result (STP).

Small size (8-20 tasks)					
Problem(no.of task)	Algorithm	PSO	ACO	SA	GA
Bowman(8)	Min. Fitness	0.9443	0.8166	0.9443	0.8166
	Max.Fitness	0.9443	0.8166	0.9443	0.8193
	Mean Fitness	0.9443	0.8166	0.9443	0.8169
	Std.Deviation	0.0000	0.0000	0.0000	0.0007
	Mean Cputime	82.9557	88.0041	98.2792	89.3140
Mansoor(11)	Min. Fitness	0.7051	0.5773	0.7051	0.5773
	Max.Fitness	0.7051	0.5773	0.7051	0.5787
	Mean Fitness	0.7051	0.5773	0.7051	0.5775
	Std.Deviation	0.0000	0.0000	0.0000	0.0004
	Mean Cputime	49.3870	107.9176	161.7723	143.5887
Instance_small(20)	Min. Fitness	0.7026	0.9499	0.9443	0.8166
	Max.Fitness	0.9077	0.9513	0.9443	0.8179
	Mean Fitness	0.8120	0.9500	0.9443	0.8166
	Std.Deviation	0.0727	0.0004	0.0000	0.0003
	Mean Cputime	52.3941	131.1931	161.1315	140.1623

Table 2 EAs computational result (MTP).

Medium size (25-50 tasks)					
Problem(no.of task)	Algorithm	PSO	ACO	SA	GA
Buxey(29)	Min. Fitness	0.7138	0.6395	0.6538	0.8658
	Max.Fitness	0.9634	0.7517	0.8493	0.9268
	Mean Fitness	0.8401	0.6969	0.7906	0.8800
	Std.Deviation	0.0454	0.0272	0.0354	0.0171
	Mean Cputime	101.4522	101.7651	2346.7180	243.4568
Gunther(35)	Min. Fitness	0.5888	0.7368	0.5842	0.8318
	Max.Fitness	0.9742	0.8427	0.8743	0.9671
	Mean Fitness	0.7973	0.7792	0.6199	0.9242
	Std.Deviation	0.1101	0.0351	0.0673	0.0599
	Mean Cputime	137.1709	136.9874	657.1917	153.3631
Instance_medium(50)	Min. Fitness	0.5673	0.6888	0.6499	0.6182
	Max.Fitness	0.7318	0.8304	0.7834	0.7723
	Mean Fitness	0.6359	0.7600	0.5162	0.6106
	Std.Deviation	0.0464	0.0404	0.0382	0.0697
	Mean Cputime	276.8158	337.7413	658.4571	405.0386

Table 3 EAs computational result (LTP).

Large size (65-100 tasks)					
Problem(no.of task)	Algorithm	PSO	ACO	SA	GA
Wee-mag(75)	Min. Fitness	0.6947	0.6475	0.6742	0.6105
	Max.Fitness	0.8411	0.7859	0.8247	0.7595
	Mean Fitness	0.7690	0.7513	0.7230	0.6777
	Std.Deviation	0.0397	0.0329	0.0393	0.0458
	Mean Cputime	1038.8310	1024.2880	1090.0520	1365.3380
Arc(83)	Min. Fitness	0.5274	0.3807	0.5279	0.7264
	Max.Fitness	0.6475	0.4835	0.6503	0.9647
	Mean Fitness	0.5903	0.4412	0.5832	0.7953
	Std.Deviation	0.0316	0.0286	0.0290	0.0614
	Mean Cputime	1632.6530	2631.1140	3044.7990	6313.9020
Instance_large(100)	Min. Fitness	0.5527	0.4858	0.4974	0.5772
	Max.Fitness	0.7298	0.6743	0.7358	0.8384
	Mean Fitness	0.6525	0.6107	0.6161	0.7012
	Std.Deviation	0.0507	0.0510	0.0710	0.0874
	Mean Cputime	2148.1490	2389.1640	2897.1870	3650.2650

Then, from the final result of fitness function, a

convergence graph can be plotted. Figure 2 displayed the convergence of fitness value for STP, MTP, and LTP respectively. Clearly from the graph, there is a variation in term of how fast these three problem converge for their respective fitness functions. STP converge is the fastest followed by MTP and LTP. This is understandable considering the number of tasks involved in each category which LTP consist the largest number of tasks. This bring into a statement that the larger the number of tasks, the longer the time it takes to converge.

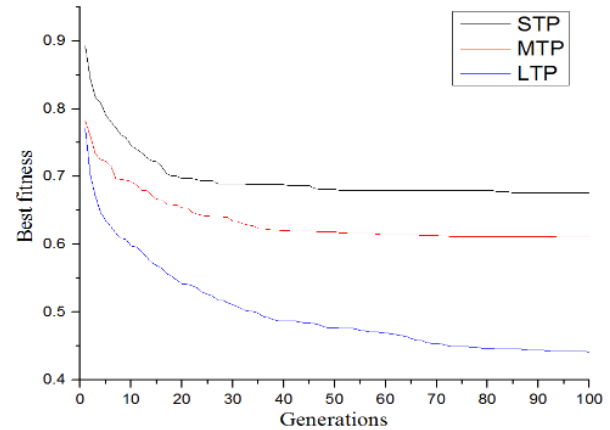


Figure 2 Convergence of fitness function.

### 4. CONCLUSIONS

The performance represented by fitness function and processing time of four evolutionary algorithms (ACO, PSO, GA, and SA) in MMALBP with resources constraint has been presented. The comparison between these EAs were made and selected objective functions has been evaluated. One of the significant findings to emerge from this study suggested that ACO algorithm performed better in each category when tested using t-test with 95% confidence level. It has produces better solution quality than PSO which ranked second, GA in third, and SA fourth.

The present study, however, has some limitation included the number of test problem being used which is if being increased can possibly return a better solution quality over generation. Further investigation also can be implement by consider actual assembly line such as manufacturing industry. Based on listed limitation, a further experimentation to measure the performance of these four EAs is strongly recommended. A number of possible future studies using the same experimental set up are apparent. It would be interesting to assess the effects of increasing the number of test problem to the solution quality produced as well as the final outcome when applying this optimization algorithm to the actual problems in an actual assembly line.

### ACKNOWLEDGEMENT

This research has been supported by research fund from Ministry of Higher Education under RDU140103.

### REFERENCES

- [1] Z. Yuguang, A. Bo, Z. Yong, "A PSO algorithm for multi-objective hull assembly line balancing using

- the stratified optimization strategy,” *Computers & Industrial Engineering*, vol. 98, pp. 53-62, 2016.
- [2] I. Kucukkoc, D. Z. Zhang, “Mathematical model and agent based solution approach for the simultaneous balancing and sequencing of mixed-model parallel two-sided assembly lines,” *International Journal of Production Economics*, vol. 158, pp. 314–333, 2014.
- [3] X. Zhao, C.-Y. Hsu, P.-C. Chang, L. Li, “A genetic algorithm for the multi-objective optimization of mixed-model assembly line based on the mental workload,” *Engineering Applications of Artificial Intelligence*, vol. 47, pp. 140–146, 2016.
- [4] M.M. Razali, M. Fadzil, F. Ab, M. Razif, “Mathematical modelling of mixed-model assembly line balancing problem with resources constraints,” *IOP Conference Series: Materials Science and Engineering*, vol. 160, no. 1, p. 012002, 2016.

# Design of high gain co-planar waveguide fed staircase shaped monopole antenna with modified ground plane for radio-frequency (RF) energy harvesting application

Alphonsos A Masius, Yan Chiew Wong\*

Faculty of Electronic and Computer Engineering, Universiti Teknikal Malaysia Melaka,  
Hang Tuah Jaya, 76100 Durian Tunggal, Melaka, Malaysia

\*Corresponding e-mail: ycwong@utem.edu.my

**Keywords:** High gain miniature antenna; RF energy harvesting; low profile antenna

**ABSTRACT** – A compact co-planar waveguide (CPW) fed monopole antenna is designed and optimized to resonate at 5.85 GHz Wi-Fi frequency band. The proposed antenna with small size of 40mm x 30mm x 1 mm is composed of a staircase shaped radiating element fed by a CPW feed line, and an inverted stair-style ground. The antenna yields a high gain of 4.152 dB and wide bandwidth of 1.63 GHz. The lengths of feedline and ground radiating elements are optimized through parametric sweep to obtain the best desirable results. The performance of the antenna is evaluated for feasibility in energy harvesting applications.

## 1. INTRODUCTION

The RF energy harvesting is developed for harvesting and recycling the ambient RF energy that is widely broadcasted by many wireless systems such as mobile communication systems, Wi-Fi base stations, and wireless portable devices. Antenna is used to detect the ambient energy then convert it to DC power by the rectification circuit. CPW fed monopole antenna is a compact wideband antenna that is easy to fabricate and integrate with any RF and MIC/MMICs communication devices [1]. However, this antenna often suffers low gain and modifications is needed to create a deep resonance. Thus, we focus on ground plane modifications of a staircase shaped monopole antenna to increase gain at 5.85 GHz Wi-Fi band for energy harvesting application.

## 2. METHODOLOGY

Figure 1 shows the geometry of the CPW staircase antenna. The return loss of the antenna must be below -10 dB to ensure the proposed antenna can achieve at least 90% matching efficiency [2]. The antenna is modelled and simulated on Computer Simulation Technology (CST) by using Rogers RT5880LZ dielectric substrate with dielectric constant,  $\epsilon_r = 1.96$ , tangent loss,  $\tan \delta = 0.002$  and substrate's thickness of 1.0mm. The staircase radiating element consists of eight rectangles of lengths  $L1 - L8$  and widths  $W1 - W8$ . The ground plane consists of combination of eight rectangles of lengths  $L9 - L16$  and widths  $W9 - W16$  on either side of the transmission line,  $Lf$ . The gap between the main patch to the ground is given as  $d$ , while the strip width of the CPW is labelled as  $Wf$  and the gap of the CPW is labelled as  $G$ , while the

substrate length,  $Lp$  is 40mm and its width,  $Wp$  is 30mm.

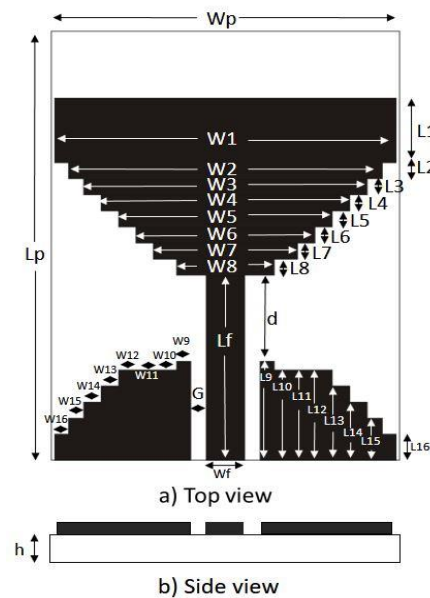


Figure 1 The geometry of the CPW staircase antenna.

The design process started by calculating the feedline strip width ( $Wf$ ) of the CPW using standard equations for 50Ω impedance [3-4]. The length of the feedline,  $Lf$  is  $\lambda/4$  at 5.85GHz. Equation (1) - (3) are used to approximate the width ( $Wl$ ) and length ( $Ll$ ) of the CPW feed [5].

$$W = \frac{c}{2f_0 \sqrt{(\epsilon_r + 1)/2}} \quad (1)$$

$$L = \frac{1}{2f_r \sqrt{\epsilon_{eff}} \sqrt{\mu_0 \epsilon_0}} - 2\Delta L \quad (2)$$

Where  $\Delta L$  is given as:

$$\Delta L = 0.412 h \frac{(\epsilon_{eff} + 0.3) \left( \frac{W}{h} + 0.364 \right)}{(\epsilon_{eff} + 0.258) \left( \frac{W}{h} + 0.8 \right)} \quad (3)$$

The calculated value of length  $L1$  and width  $W1$  are used to find the values of the next  $L2-L8$  and  $W2-W8$  through parametric study. The next length  $L2$  is reduced from  $L1$  through parameter sweep to optimize the antenna gain and bandwidth, and is repeated for the next corresponding  $L3-L9$  until no further significant increases in gain and bandwidth are detected. The ground patch is a mirror image of the main patch. The

value of  $W_f$  and  $d$  are then optimized through parameter sweep to obtain a resonant frequency at 5.85 GHz.

### 3. RESULTS AND DISCUSSION

Table 1 shows the original and optimized parameters for lengths, widths,  $d$ , and  $G$  at 5.85 GHz.

Table 1 The original and optimized antenna parameters.

Parameter	Original (mm)	Optimized (mm)
L1	6	6
L2-L3	NA	1.5
L9	12.95	9.2
L10	11.4	8.4
L11	9.9	8.4
L12	8.4	8.4
L13	6.9	6.9
L14	5.4	5.4
L15	3.9	3.9
L16	2.4	2.4
W1	29.4	29.4
W2	27.0	27.0
W3	24.4	24.4
W4	21.4	21.4
W5	18.4	18.4
W6	15.4	15.4
W7	12.4	12.4
W8	8.4	8.4
G	1.345	1.0
Lf	12.81	17.25
Wf	3.31	3.31
d	2.8	8.050

During the optimization, it is observed that decreasing  $L_9$  shifted the resonant frequency to the right and vice versa, and the value of  $d$  correspond to  $L_9$ .  $W_f$  is optimum at the calculated value while increasing it worsen the matching at  $50\Omega$ . The antenna shows significant increases in gain and depth of resonance when  $L_f$  is increased from 12.81 to 15.75mm. However, when the  $L_f$  further increases to 17.25mm, the depth of resonance decreased but the resonance frequency shifted closer to 5.85 GHz and the gain is further increased. The return loss of the optimized and original antenna design is shown in Figure 2. It is shown that the antenna has a wide bandwidth of 1.63 GHz ranging from 5.21 GHz to 6.84 GHz. The gain at 5.85 GHz is 4.152 dB which is higher than monopole antennas listed in [1]. With such gain, this enable energy harvesting in close distance between the antenna and base station, according to the Friis equation as stated in [6]. The antenna is small in size with overall dimension of 40mm x 30mm x 1 mm.

### 4. CONCLUSIONS

This paper focuses on optimizing the lengths of feedline and ground radiating elements to increase gain at 5.85 GHz. The antenna is low-profile with dimension of 40mm x 30mm x 1 mm with gain of 4.152 dB which is higher than most of the monopole antennas with same

size range that have peak gain in the range of 1 – 3 dB [1]. The proposed antenna also shows high feasibility for close distance energy harvesting from Wi-Fi routers.

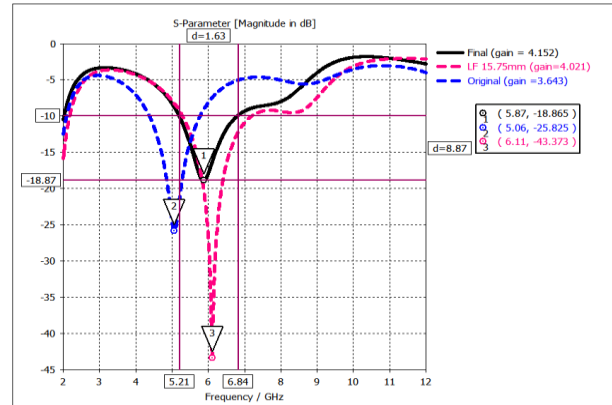


Figure 2 Return loss of the optimized and original antenna design.

### ACKNOWLEDGEMENT

The authors gratefully acknowledge the financial support by Universiti Teknikal Malaysia Melaka and Ministry of Higher Education under research grant no. RAGS/1/2015/TK0/FKEKK/02/B0099.

### REFERENCES

- [1] P. V. Naidu & A. Malhotra, "A compact stair case shaped monopole dual band antenna for bluetooth/WLAN and UWB applications," *Int. J. Microw. Opt. Technol.*, vol. 11, no. 1, pp. 64–71, 2016.
- [2] K. Ismail & S. H. Ishak, "Sierpinski gasket fractal antenna with defected ground structure (DGS)," *Int. Conf. ICT Converg.*, pp. 441–446, 2012.
- [3] V. A. Shameena, S. Jacob, C. K. Aanandan, K. Vasudevan, & P. Mohanan, "A compact CPW fed serrated UWB antenna," *ICCSP 2011 - 2011 Int. Conf. Commun. Signal Process.*, pp. 108–111, 2011.
- [4] Y. C. Wong, T. Arslan, & A. T. Erdogan, "Reconfigurable wideband RF impedance transformer integrated with an antenna for multi-band wireless devices," in *Loughborough Antennas and Propagation Conference*, 2012, no. November.
- [5] I. Rafiqul, M. Ieee, A. A. H. M. Zahirul, S. M. Ieee, & M. F. A. J. Khan, "Design of Microstrip Patch Antenna Using Slotted Partial Ground And Addition Of Stairs And Stubs For UWB Application," *Cyber Journals Multidiscip. Journals Sci. Technol. J. Sel. Areas Telecommun.*, pp. 1–8, 2012.
- [6] M. Arrawatia, M. S. Baghini, & G. Kumar, "RF energy harvesting system from cell towers in 900MHz band," *2011 Natl. Conf. Commun. NCC 2011*, 2011.



# Design of wide tuning CMOS voltage controlled ring oscillator for reconfigurability DC-DC converter

Mohamad Khairul Mohd Kamel, Yan Chiew Wong\*

Faculty of Electronic and Computer Engineering, Universiti Teknikal Malaysia Melaka, Hang Tuah Jaya, 76100 Durian Tunggal, Melaka, Malaysia

\*Corresponding e-mail: ycwong@utem.edu.my

**Keywords:** Voltage controlled ring oscillator; wide tuning range; dc-dc converter

**ABSTRACT** – Generating wide tuning range of frequency clock generator is crucial for dc-dc converter block. Current starved voltage controlled ring oscillator (CSVCRO) usually have wide tuning range, occupy less on-chip integration area which makes them being more widely used than other types of oscillator. This paper represents the design and evaluation of performance wide tuning range CSVCRO. The analysis on the performance of CSVCRO has been compared with VCRO controllable resistor (RVCRO). The circuit is designed using 180nm CMOS technology. By varying input voltage, wide tuning range has been observed from 6.7MHz to 208MHz.

## 1. INTRODUCTION

A voltage-controlled oscillator (VCO) is considered as one of the important building blocks in analog and digital circuits [1-3]. There are many different implementations of VCOs. One of them is a ring oscillator based VCO, which is commonly used in the clock generation subsystem. The main reason for ring oscillator popularity is its easy integration [2- 5].

The design of a ring oscillator requires connecting an odd number of inverters and feedback from the output of the last one to the input of the first one [2-4]. The design of conventional delay cell is shown in Figure 1. The oscillation frequency is determined by the number of stages and the delay in each stage. Increasing the number of stages give a lower frequency while reducing the number of stages will result in high frequency. Many research has been done to increase delay for each stage without increasing the number of stages. If the delay is voltage controllable, then a VCO with variable-frequency output is obtained [1].

Therefore, in this paper, an analysis on the voltage controlled ring oscillator with current starved delay cell is evaluated. The output frequency is not stable when it is a VDD dependent. Implemented of current starved delay cell supply current to each inverter instead of VDD. In the dc-dc converter, a good performance of VCO is very important to avoid the degradation of the output voltage since frequency is important parameters influence the performance of the converter [5]. Input clock signal with high frequency result in low output voltage while low frequency will produce a high output voltage.

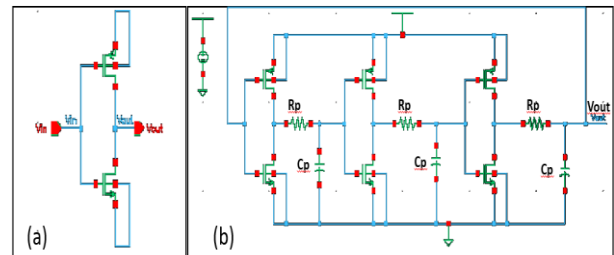


Figure 1 (a) Basic VCO based on inverter circuit (b) RVCRO circuit.

The organisation of the paper is arrange as follows. Section 2 present the circuit design of current starved voltage controlled ring oscillator. Section 3 shows simulation results and the discussion on the performance analysis and section 4 concludes the work.

## 2. METHODOLOGY

The circuit design of CSVCRO is shown in Figure 2. The circuit has been designed using Cadence tool with 180nm CMOS technology. From the schematic there is implementation of PMOS and NMOS in each delay cell and the design is fixed to five stages.

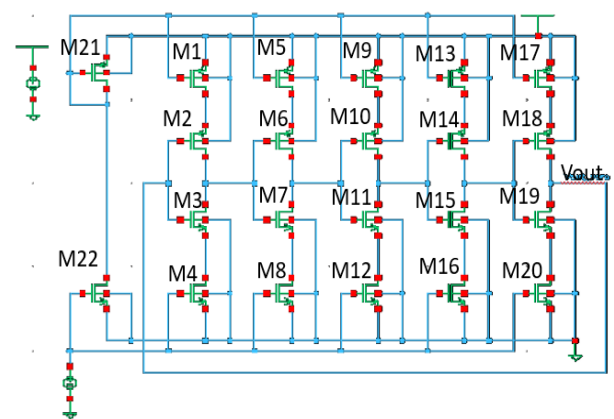


Figure 2 CSVCRO schematic.

The roles of transistor M2 and M3 in delay cells is to have a function of an inverter while the M1 and M4 function as different current sources. The inverters are consuming very high current, so with the help of transistors M1 and M4 the current will be limited. Frequency must be depended on a control parameter in order to convert an oscillator into voltage controlled

oscillator. In this work, control voltage is set as the control parameter. For schematic in Figure 1(b), based on equation 1, frequency is depending on the controlled resistor.

$$f_{osc} = \frac{g_m}{2NC_p(1+g_mR_p)} \quad (1)$$

Where  $f_{osc}$  is oscillator frequency,  $g_m$  is transconductance,  $N$  is a number of stages,  $C_p$  is capacitance and  $R_p$  is resistance.

### 3. RESULTS AND DISCUSSION

Figure 3(a) shows the transient analysis of CSVCRO at 1.8V supply voltage with an input control voltage of 2.5V. The obtained frequency is 138MHz. While in Figure 3(b) shows transient analysis for RVCRO at 1.8V and the observed frequency is 12.37MHz. Clipping on the signal has been observed in Figure 3(a) due to high switching frequency. This has been discussed in Section 2 where the current has been limited to the inverter. Therefore, the tops of the waves get clipped off.

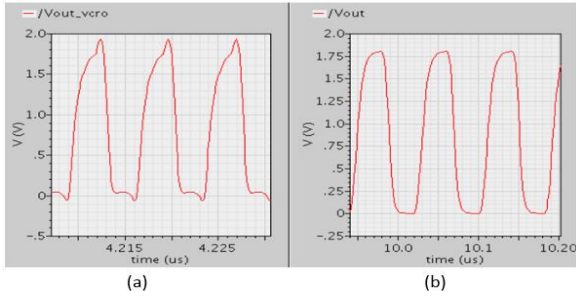


Figure 3 Transient analysis (a) CSVCRO (b) RVCRO.

Figure 4 represents graphically of the variation frequencies over input voltage. The input voltage has been varied from 0.5V to 3V. This proposed designed has been compared with the RVCRO. Observation based on Figure 4 shows that CSVCRO has successfully computed wide tuning range frequency compared to RVCRO. The phase noise of CSVCRO is investigated and it is measured at 1 MHz offset frequency as shown in Figure 5(a). The phase noise for minimum frequency is -112.4dBc/Hz while -115.6dBc/Hz for maximum frequency. There is no significant change of the phase noise over the frequency. However, the power dissipation shows an increasing when the frequency increase. At minimum frequency, the power dissipation is 1.15μW while 2.05mW at maximum frequency as shown in Figure 5(b).

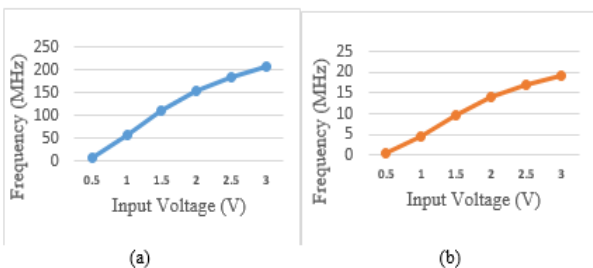


Figure 3 Input voltage versus Frequency (a) CSVCRO (b) RVCRO.

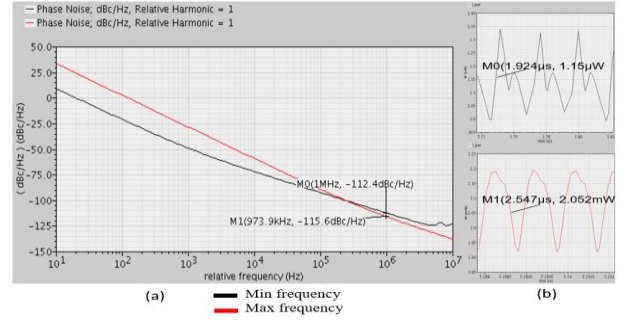


Figure 5 (a) Analysis of phase noise (b) power dissipation.

### 4. CONCLUSION

In this paper, CSVCRO has been designed and evaluated to compute wide tuning range frequency. CSVCRO has shown a wide tuning range compared to RVCRO. The CSVCRO frequency has been tuned from 6.7MHz to 208MHz while for RVCRO is 0.34MHz to 19.4MHz. In other words, that CSVCRO expands in hundred times of Mega Hz. Analysis on phase noise shows slightly change over frequency. However, increasing the frequency will result in higher power dissipation. Obtaining a wide tuning frequency of CSVCRO enables highly reconfigurable in a DC-DC converter.

### ACKNOWLEDGMENT

The authors acknowledge the financial support by Universiti Teknikal Malaysia Melaka and Ministry of Higher Education MOHE research grant No. RAGS/1/2015/TK0/FKEKK/02/B00099.

### REFERENCES

- [1] J. Ren, K. El-Sankary, and E. El-Masry, "Design of low-voltage wide tuning range CMOS multipass voltage-controlled ring oscillator," *53rd IEEE International Midwest Symposium on Circuits and Systems*, pp. 109-112, 2010.
- [2] V. Michal, "On the low-power design, stability improvement and frequency estimation of the CMOS ring oscillator," *22nd Int. Conf. on Radioelektronika*, pp. 1-4, 2012.
- [3] V. Sikarwar, N. Yadav, and S. Akashe, "Design and analysis of CMOS ring oscillator using 45 nm technology," *Proc. 2013 3rd IEEE Int. Adv. Comput. Conf.*, vol. 2, no. 2, pp. 1491-1495, 2013.
- [4] M. Bhardwaj and S. Pandey, "Design and performance analysis of wideband CMOS voltage controlled ring oscillator," *2nd Int. Conf. Electron. Commun. Syst.*, pp. 142-145, 2015.
- [5] Y. C. Wong, T. Arslan, A. T. Erdogan, and A. O. El-rayis, "Efficient ultra-high-voltage controller-based Efficient ultra-high-voltage controller-based switched-capacitor DC – DC converter for radio-frequency micro-electro-mechanical systems switch actuation," *IET Circuits, Devices & Systems*, vol. 7, no. 2, pp. 59-73, 2013.

# Evaluation of mechanical properties for open cellular structure 17-4 PH stainless steel alloy fabricated by selective laser melting process

M.F.F.A. Hamidi, W.S.W. Harun\*

Human Engineering Group, Faculty of Mechanical Engineering, Universiti Malaysia Pahang,  
26600 Pekan, Pahang, Malaysia

\*Corresponding e-mail: sharuzi@ump.edu.my

**Keywords:** Selective laser melting; 17-4 PH stainless steel; open cellular structure

**ABSTRACT** – Additive layer manufacturing processes technology especially selective laser melting process has offered capabilities to produce samples with excellent mechanical properties. In this study, samples of 17-4 PH Stainless Steel open cellular structure with various volume porosity ranging between 60% and 90% has been fabricated using direct metal laser sintering process. The mechanical properties were determined through uniaxial compression and hardness testing. The 60% volume porosity sample showed the optimum compressive strength and modulus of elasticity compared to 70%, 80% and 90% volume porosity for the compression test. For hardness test, the different surface area seems does not affect the hardness value of the samples.

## 1. INTRODUCTION

Selective laser melting (SLM) was developed in the late 1990s as an economic layer-by-layer near-net-shape process allowing for fabricating near fully dense metal components with complex geometries by selectively melting successive layers of metal powders from various materials [1-2]. It is a powder bed fusion (PBF) process of AM technologies which refer to a group of technologies used for tooling parts, building physical models, prototypes, and functional parts, all from 3D computer-aided design (CAD) data or 3D scanning systems data, medical scanners, or other geometry representations [3]. Selective laser melting utilises a fiber laser heat source. There are several main parameters in SLM process which are scan speed, laser power, hatch spacing, point distance, focal diameter, exposure time and layer thickness. The process is characterised by high scanning speeds and high thermal gradients, leading to high cooling rates. High cooling rates result in non-equilibrium microstructures which required heat treatment for particular applications. The SLM build chamber is continuously filled with inert gas especially nitrogen to reduce oxygen content. Common layer thickness lies in the range of 20-100  $\mu\text{m}$  [4].

SLM process allows complex 3D lattice structures to be created while also lowering the costs and time of production. This technology allows flexibility of design and provide very few feature sizes for fabricating closed or open cell structures with locally variable stiffness and optimised compatibility [5]. In term of material selection, SLM has some limitation. It is limited because extensive investigations into appropriate process parameter combinations for each different material are needed.

Common materials which are currently available for SLM include alloys such as Ti-6Al-4V, 316L stainless steel, 304 stainless steel, 17-4 PH stainless steel, Inconel 625, M2 high-speed steel, Ni718, and CoCr alloys [6-7].

17-4PH stainless steel is typically used in a wide range of areas including commercial, defence and medical industries. Martensite and metastable austenite are common phases observed in samples fabricated by SLM processing. The objective of this study is to evaluate the mechanical properties for open cellular structure 17-4 PH stainless steel alloy fabricated by selective laser melting. Compression test and hardness test have been performed to determine the compressive properties and hardness of open cellular structures.

## 2. METHODOLOGY

Water-atomized, pre-alloyed 17-4 PH powder was used as the working material to fabricate open cellular structure samples. All samples in this work were divided into four group which is based on their percentage of volume porosity. The designed volume porosity of the samples was designed to vary between approximately 60% and 90%. CAD design for the four individual open cellular structures with different porosity was created by using the Solid Works software. The wall thickness of an open cellular structures samples will be in a range of 0.3mm to 0.65mm with pore sizes in a lattice shape. The samples were manufactured using an EOSINT M280 machine operated on PSW 3.06 software. The powder was manually sieved. All samples were built using 20  $\mu\text{m}$  layers thickness and the process parameters used for this work comprised of a laser power 195 W, 0.1 mm scanning space, and laser scan speed of 1000 mm/s. The fabrication chamber was filled with nitrogen gas with less than 1.3 % oxygen present.

Four samples condition with different porosity, i.e. 60, 70, 80 and 90% were tested under compression in accordance with the ISO standard for mechanical testing of porous metallic materials, ISO 13314:2011 with a maximum load capacity of 100kN. The samples fabricated by selective laser melting process were loaded to 1 mm displacement as the maximum strut size set is 0.92 mm. The open cell samples were elastic tested at a stroke rate of 0.1 mm/min and the acquired real time mechanical testing data were recorded on a PC for further analysis. Hardness tests employed the micro Vickers hardness on MMT X7 hardness test machine. Time taken for each indentation were 10 seconds, and the load were set

between 1 to 500gf. Two sample with different surface area which is from top and side surface of building direction were undergone the testing

### 3. RESULTS AND DISCUSSION

#### 3.1 Compressive strength

The mean compressive strength was determined from the real-time force versus displacement data and typical stress-strain relationship for each design volume porosity is shown in Figure 1.

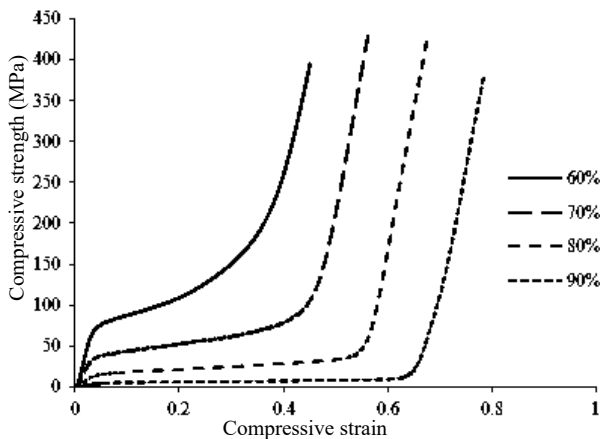


Figure 1 Stress-strain relationship for each design volume porosity.

The 0.2% proof strengths and compressive elastic modulus were both decrease with the increase in volume porosity. The mean 0.2% proof strength varied between 2.9 MPa and 61 MPa and the mean compressive elastic modulus varied between 0.12 GPa and 2.39 GPa.

#### 3.2 Hardness test

For hardness test, five number of point were indented on the side and top surface. The comparison for mean average are shown in Figure 2.

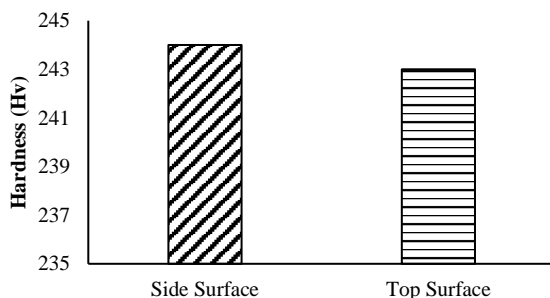


Figure 2 Mean average for hardness value.

The mean average for side and top surface were recorded at 244 HV and 243 HV. The hardness value for side surface demonstrated 0.4 % greater than the top surface. So it can be concluded that there are no major differences of hardness value between both surfaces.

### 4. CONCLUSION

For the experimental result, it been shown that for a compression test, 60% volume porosity recorded highest compressive strength and elastic modulus compared to 70%, 80% and 90% volume porosity due to its bigger strut size and higher solid region. The wall thickness and strut size play the most important role to determine the strength of the sample. For the hardness test, the different surface area does not give any significant effect on the hardness values.

### ACKNOWLEDGEMENT

We would like to thank Universiti Malaysia Pahang through grant GRS1503115, GRS1503121 (UMP grant) and RDU151314 (RACE) for fully supports the facilities and resources for this research.

### REFERENCES

- [1] A. Mertens, S. Reginster, Q. Contrepolis, T. Dormal, O. Lemaire, and J. Lecomte-Beckers, "Microstructures and mechanical properties of stainless steel AISI 316L processed by selective laser melting," in *Materials Science Forum*, vol. 783, no. 786, pp. 898-903, 2014.
- [2] C. Yan, L. Hao, A. Hussein, P. Young, J. Huang, and W. Zhu, "Microstructure and mechanical properties of aluminium alloy cellular lattice structures manufactured by direct metal laser sintering," *Materials Science and Engineering: A*, vol. 628, pp. 238-246.
- [3] E. Yasa and J. P. Kruth, "Microstructural investigation of Selective Laser Melting 316L stainless steel parts exposed to laser re-melting," *Procedia Engineering*, vol. 19, pp. 389-395, 2011.
- [4] J. Cherry, H. Davies, S. Mehmood, N. Lavery, S. Brown, and J. Sienz, "Investigation into the effect of process parameters on microstructural and physical properties of 316L stainless steel parts by selective laser melting," *The International Journal of Advanced Manufacturing Technology*, vol. 76, pp. 869-879, 2015.
- [5] H. Alsalla, L. Hao, and C. Smith, "Fracture toughness and tensile strength of 316L stainless steel cellular lattice structures manufactured using the selective laser melting technique," *Materials Science and Engineering: A*, vol. 669, pp. 1-6, 2016.
- [6] H. K. Rafi, D. Pal, N. Patil, T. L. Starr, and B. E. Stucker, "Microstructure and Mechanical Behavior of 17-4 Precipitation Hardenable Steel Processed by Selective Laser Melting," *Journal of Materials Engineering and Performance*, vol. 23, pp. 4421-4428, 2014.
- [7] B. Song, S. Dong, S. Deng, H. Liao, and C. Coddet, "Microstructure and tensile properties of iron parts fabricated by selective laser melting," *Optics & Laser Technology*, vol. 56, pp. 451-460, 2014.

# The effect of cutting parameters on tool wear in end milling of AISI D2 tool steel

N.H.J. Luqman<sup>1,\*</sup>, S. Mohd Shukor<sup>2</sup>, M. Hadzley<sup>2</sup>

<sup>1)</sup> Politeknik Muazam Shah, Lebuhraya Tun Abdul Razak, 26700 Muadzam Shah, Pahang, Malaysia

<sup>2)</sup> Faculty of Manufacturing Engineering, Universiti Teknikal Malaysia Melaka, Hang Tuah Jaya, 76100 Durian Tunggal, Melaka, Malaysia

\*Corresponding e-mail: luqmannulhakim@gmail.com

Keywords: Dry milling; tool wear; Taguchi method

**ABSTRACT-** Tool wear has become a very significant consideration in order to achieve optimum cutting parameter in the hard milling process. This experiment is conducted to study the effect of cutting parameters on tool wear of AISI D2 tool steel using TiAlN coated carbide endmill. CNC Milling is used in this project to remove the material surface by applying dry milling process. The selected parameters are cutting speed, feed rate and depth of cut and the cutting parameter that has been designed by the Taguchi Method L9 orthogonal array. The tool wear of cutting tool is analysed using a stereo microscope. The result shows that development of tool wear appeared at the edge of cutting tool with flank and crater wears dominate the failure modes.

## 1. INTRODUCTION

Ability to produce complex shapes, fine surface roughness and higher material removal rate makes hard milling has broad application in mould and die industries. Due to the fact that, when machining performed at dry condition, the friction and sliding between chip and tool tend to be higher which causes high temperatures, high wear rates and shorter tool lives [1]. Instead of seeming to be more economical, machining in dry condition should be applied at controlled parameters to avoid excessive wear. Pantazopoulos et al. stated that the main cutting tool abnormal failure modes in their study to the following classes such as notch damage, fracture, breakage, chipping, flaking, welding, plastic deformation and thermal cracking [2].

In this study, 10 mm diameter TiAlN coated carbide endmill used to mill AISI D2 tool steel based on cutting parameter that has been designed by the Taguchi Method L9 orthogonal array. The general purpose of this study is to expand the knowledge of tool wear in the hard milling process.

## 2. EXPERIMENTAL PROCESSES

The cutting tools that used in this project are 10 mm diameter TiAlN coated carbide endmill. The workpiece material selected was AISI D2 tool steel workpiece in the square shape of 50 mm width x 40 mm length x 30 mm thickness. The machining trials were carried out by using HAAS CNC Milling 3 Axis.

The parameters used and the experimental design is shown in Table 1 and Table 2.

Table 1 The machining cutting parameter.

Factor	Unit	Level 1	Level 2	Level 3
A Cutting Speed	m /min	150	200	250
B Feed Rate	mm /tooth	0.005	0.010	0.015
C Depth of Cut	mm	0.1	0.2	0.3

Table 2 Orthogonal array design.

No. of Exp.	Designation	Cutting Speed (m/min)	Feed Rate (mm/tooth)	Depth of Cut (mm)
1	A1B1C1	150	0.005	0.1
2	A1B2C2	150	0.010	0.2
3	A1B3C3	150	0.015	0.3
4	A2B1C2	200	0.005	0.2
5	A2B2C3	200	0.010	0.3
6	A2B3C1	200	0.015	0.1
7	A3B1C3	250	0.005	0.3
8	A3B2C1	250	0.010	0.1
9	A3B3C2	250	0.015	0.2

After all face milling operations done, the TiAlN coated carbide endmill was removed from the tool holder and the generated tool wear on the endmill was measured using a stereo microscope. The wear image was captured and it was measured on the computer monitor using the measurement software.

## 3. RESULTS AND DISCUSSION

Table 3 shows the experimental result of tool wear. As shown in Figure 2, the maximum size of flank wears recorded for experiment 3 with  $V_b = 0.326$  mm. For crater wear, maximum size recorded was at the experiment 7 with  $V_c = 0.23$  mm. The minimum size of the flank and crater wear were clearly shown in experiment number 2 with  $V_b = 0.016$  mm and  $V_c = 0.009$  mm as shown in Figure 3. This shows that set of parameters from experiment 2 demonstrate optimum results for wear performance. The optimum parameter of this experiment is observed by the lowest value of tool wear with a combination of cutting speed is 150 m/min, feed rate is 0.010 mm/tooth and depth of cut is 0.2 mm.



Table 3 Experimental result of tool wear.

No. of Exp.	Flank Wear, Vb (mm)	Crater Wear, Vc (mm)
1	0.084	0.152
2	0.016	0.009
3	0.326	0.065
4	0.279	0.109
5	0.298	0.140
6	0.105	0.124
7	0.301	0.230
8	0.195	0.140
9	0.242	0.152

Figure 2 shows the flank wear and crater wear observed using a stereo microscope under 2.5x magnification. Due to friction between machined surface and cutting tool, loss of tool edge could increase the cutting force and rotational vibration of the cutting tool. This would increase the risk of another failure, such as chipping and fracture, which devastated to the machining performance.

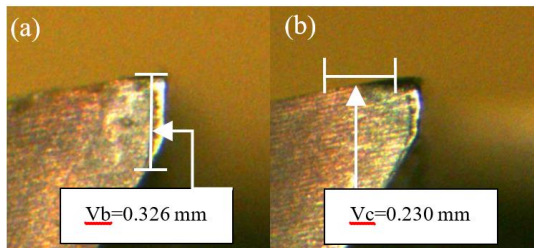


Figure 2 (a) Maximum flank wear in experiment 3  
(b) Maximum crater wear in experiment 7.

When the cutting parameters applied correctly, minimum wear should be appeared as shown in Figure 3. Minimum wear probably due to lower contact area, which indicates the machining can be prolonged to improve productivity.

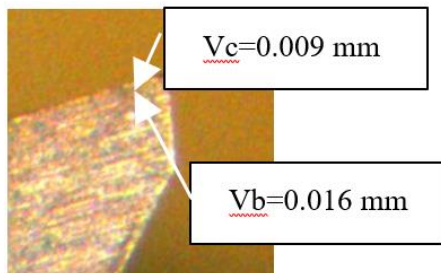


Figure 3 Minimum flank/crater wears in experiment 2.

Figure 4 shows the graph of flank wear and crater wear versus feed rate and depth of cut. Each graph (a), (b) and (c) are separated by different cutting speed which is the cutting speed for Figure 4 (a) is 150 m/min, Figure 4 (b) is 200 m/min and Figure 4 (c) is 250 m/min. From the graph in Figure 4 (b) and (c) shows that the flank and crater wear is increased when the value of depth of cut is increased.

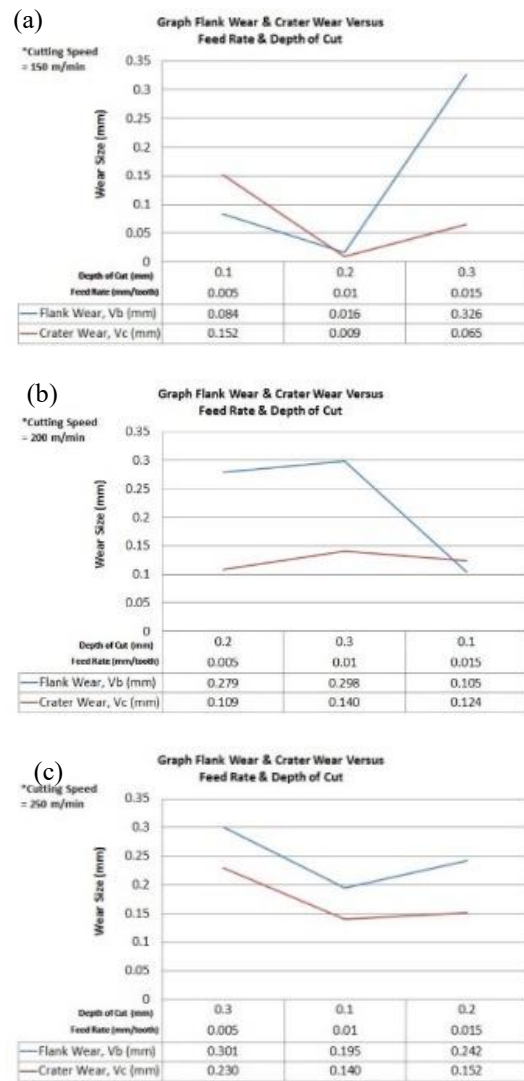


Figure 4. Plots of feed and cutting depth for the cutting speeds (a) 150 m/min (b) 200 m/min (c) 250 m/min.

#### 4. CONCLUSIONS

The conclusion are the dominant wear modes shown in the experiment are flank wear and crater wear. Then, the optimum values for lowest tool wear are cutting speed which is 150 m/min, the feed rate is 0.010 mm/tooth and the depth of cut is 0.2 mm. The depths of cut have a significant influence on the tool wear rate.

#### REFERENCES

- [1] S. Sulaiman, M.K.A. Ariffin, R.M. Norsat, "Influence of dry machining parameters in minimization of tool wear", *International Conference on Advances in Engineering Sciences & Applied Mathematics*, vol. 3, pp. 102-105, 2015.
- [2] G. Pantazopoulos, A. Toulfatzis, A. Vazdirvanidis, A. Rikos, "Accelerated carbide tool wear failure during machining of hot work hardened tool steel", *International Journal of Structural Integrity*, vol. 6, pp. 290-299, 2015.

# The effect of machining strategies on dimensional accuracy in flank milling for five-axis slanted thin-walled – aero structural component

S.A. Sundi<sup>1,2,\*</sup>, M.S. Jumali<sup>1,2</sup>, M.R.M. Razly<sup>1</sup>, M.F.A. Rob<sup>2</sup>, R. Izamshah<sup>1</sup>, M.S. Kasim<sup>1</sup>

<sup>1)</sup> Advanced Manufacturing Centre, Faculty of Manufacturing Engineering, Universiti Teknikal Malaysia Melaka, Hang Tuah Jaya, 76100 Durian Tunggal, Melaka, Malaysia

<sup>2)</sup> Faculty of Engineering Technology, Universiti Teknikal Malaysia Melaka, Hang Tuah Jaya, 76100 Durian Tunggal, Melaka, Malaysia

\*Corresponding e-mail: syahrul.azwan@utem.edu.my

**Keywords:** Dimensional accuracy; flank milling; slanted thin-walled

**ABSTRACT** –This research initiated to investigate the effect of dimensional accuracy when machining slanted thin-walled pocketing profile with various flank milling machining strategies. Multi-axis flank contouring was the main machining process used as offered by CATIA V5 software to machine an actual chosen aero-structural sample with slanted thin-walled of 105° and 85°. Two main machining strategies applied were namely Combin Parelm and Combin Tanto. Coordinate Measuring Machine (CMM) is utilized to measure the dimensional accuracy of the machined part specimens. The material was aluminum AA6063 and end mill carbide D10 was the cutting tool used. From the result obtained, Combin Parelm strategy illustrated better average sigma value than Combin Tanto. Factors affected to this result are discussed further in this paper.

## 1. INTRODUCTION

Machining of aerospace structural components involves several thin-walled rib and flange sections. These thin-walled sections are dictated by design consideration to meet required strength and weight constraints. During machining, it has been reported that the common problem for thin-walled components is dimensional surface errors as reported by Izamshah et al. [1] and Aijun and Zhanqiang [2]. The problem exists due to the deflection between specimen and cutting tool where the thin-walled is easier to deform under the enormous cutting force. In addition, the accuracy and quality of the machined wall is difficult to control due to the thicker structure at the top and thinner structure at the root of the product.

On the other hand, five-axis machining is gaining popularity as it provides additional flexibility, which can be used to improve production efficiency and quality of surface finish. In theory, the five-axis numerical control (NC) machining of sculptured surfaces can be classified into face milling and cylindrical milling (or flank milling). In practice, the flank milling suffers more difficulties than the first one, which are mostly related to gouge avoidance, interference avoidance and tool strength regardless of any types of materials [3]. Many studies have focused on improving the tool path planning of the ruled surface machining [4]. Harik et al. [5] agreed that the flank milling is very important in machining of aircraft structural parts, turbines, blades and several other

mechanical parts. They also reported that research in flank milling also focuses on the generation of optimal tool trajectory for non-developable ruled surfaces, even generic free-form surfaces.

Machining strategy is a way of machining which normally determined in the CAD/CAM programming phase. The types of machining strategy chosen is depending on machining time, surface quality and texture, and variation of the cutting forces along the tool path. Hence, an optimization can be achieved when the appropriate machining strategy is applied [6]. The selected machining strategy used in this research was multi-axis flank contouring as offered by CATIA V5 in order to machine an actual chosen aero-structural sample with slanted thin-walled of 105° and 85°. Those two angles were found to be the most common design of aero-structural components based on preliminary reviews done from available CAD models especially related to “rib” section.

## 2. METHODOLOGY

Firstly, an actual aero-structural 3D Computer Aided Design (CAD) model gone through rescaling and removing unnecessary parts in order to obtain the desired slanted thin-walled area to be studied as illustrated in Figure 1 and Figure 2.



Figure 1 Rescaling and removing process.

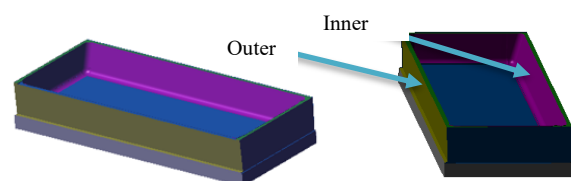


Figure 2 Final slanted inner and outer thin-walled.

Secondly, Computer Aided Manufacturing (CAM) program consist of two selected strategies namely Combin Parelm and Combin Tanto from multi-axis flank contouring process in Advanced Machining workbench is prepared. Machining parameters are remained the same for both machined part specimens

Once the CAM program completed and verified, NC codes program is generated from APT.source file. The physical machining successfully done by utilizing DMU-60 Monoblock five-axis CNC milling center. Dimensional accuracy analysis then carried out by Carl Zeiss Contura G2 Coordinate Measuring Machine (CMM). Three different areas namely top, middle and bottom area of the slanted thin-wall are taken for further analysis as shown in Figure 3 and Figure 4.

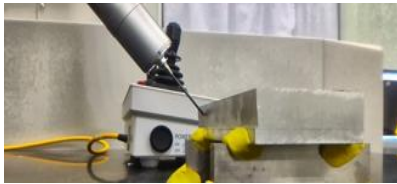


Figure 3 Dimensional accuracy data obtained by CMM.

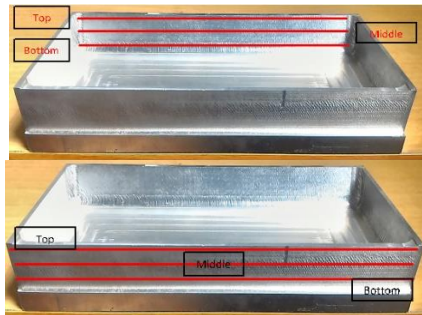


Figure 4 Final machined part specimens.

### 3. RESULTS AND DISCUSSION

From the Table 1 and Figure 5, Combin Parelm strategy exhibits slightly better result for both 85° and 105° slanted thin-walled than Combin Tanto strategy by the difference of approximately 0.72 mm or 26.55% in overall average sigma value. In theory, Combin Parelm is a strategy which the tool following the “isoparametric” of the part surface with a fanning in the beginning and at the end of the tool motion.

Table 1 Average sigma ( $\delta$ ) value.

Machining Strategy	Inner Wall avg.	Outer Wall avg.	Sum of Both Walls	Diff. (%)
	Sigma ( $\delta$ ) (mm)	Sigma ( $\delta$ ) (mm)		
<b>Combin Parelm</b>	0.56889	1.41622	1.98511	<b>26.55</b>
<b>Combin Tanto</b>	1.22611	1.47657	2.70268	

Besides, this strategy also utilizes the “isoparametric” of the drive surfaces to form a good orientation. The tool axis is tangent to the drive surface at a specified contact height and follows the “isoparametric”. The position of tool axis is strongly believed to be the main factor contributed to the obtained

result. On the other hand, Combin Tanto strategy uses minimum lead angle approach when machining flank milling surfaces. Hence, this may lead to the decreases of the chip removal effectiveness. Lead angle with optimum degree of cutting will lead to the effectiveness of chip removal and produce fine finishes [6].

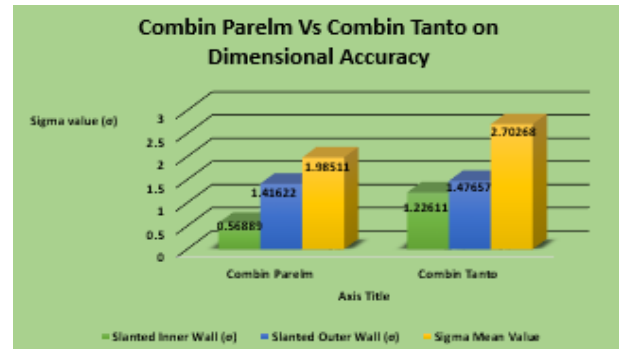


Figure 5 Histogram of dimensional accuracy based on sigma ( $\delta$ ) value.

### 4. CONCLUSIONS

This paper presented a comparison result of dimensional accuracy applying various flank milling strategies namely Combin Tanto and Combin Parelm in machining slanted thin-walled of 105° and 85°. Combin Parelm strategy illustrated better average sigma value than Combin Tanto. Tool positioning, trajectory as well as lead angle whilst performing the flank cutting were believed the main contributions towards the result obtained. As the impact of this study, industries out there especially aerospace industry are able to choose the most appropriate strategy in cutting slanted thin-walled profile as presented in this paper.

### REFERENCES

- [1] R.Izamshah, M.Y. Yuhazri, M. Hadzley, M. Amran and S. Subramanian, "Effects of end mill helix angle on accuracy for machining thin-rib aerospace component", *App. Mechanical and Materials*, vol. 315, pp. 773-777, 2013.
- [2] T. Aijun and L. Zhanqiang, "Deformations of thin-walled plate due to static end milling force", *J. of Material Processing Tech.*, vol. 6, pp. 345-351, 2007
- [3] Liu X. W. "Five-Axis NC Cylindrical Milling of Sculptured Surfaces", *Computer Aided Design*, vol. 27, pp.887-894, 1995.
- [4] S. Bedi, S. Mann, and C. Menzel, "Flank milling with flat end milling cutters," *CAD Comput. Aided Des.*, vol. 35, no. 3, pp. 293–300, 2003.
- [5] R. F. Harik, H. Gong, and A. Bernard, "5-axis flank milling: A state-of-the-art review," *CAD Comput. Aided Des.*, vol. 45, no. 3, pp. 796–808, 2013.
- [6] E. Ozturk, L. T. Tunc, and E. Budak, "Investigation of lead and tilt angle effects in 5-axis ball-end milling processes," *Int. Journal of Machine Tools & Manufacture*, vol. 49, no. 14, pp. 1053–1062, 2009.